Deformation and Seepage Characteristics of Coal Under True Triaxial Loading–Unloading

(Article begins on next page)

Deformation and seepage characteristics of coal under true triaxial loading–unloading

Chongyang Wang[1,2], Dongming Zhang [1,2], Beichen Yu [1,2], Shujian Li [2,3,4]*

1. State Key Laboratory of Coal Mine Disaster Dynamics and Control, Chongqing University, Chongqing 400030, China.

2. School of Resources and Safety Engineering, Chongqing University, Chongqing 400030, China.

3. Yunnan Phosphate Chemical Group Co., Ltd., Kunming Yunnan 650600, China

4. National Engineering and Technology Research Center for Development and Utilization of Phosphate Resources, Kunming Yunnan 650600, China

** Correspondence: zhangdm@cqu.edu.cn.*

Abstract: True triaxial loading–unloading tests of coal samples were performed using a multifunctional true triaxial fluid–solid coupling experimental system. The deformation, seepage, damage, strength, and failure characteristics of the coal samples were analyzed. Based on this, the variation mechanism of the permeability and yield conditions under different gas pressures was investigated, and the true triaxial loading–unloading of the coal sample was verified using numerical simulation software. The results show that the volumetric strain of the samples exhibited a process of compaction, flatness, and recompaction with an increase in time. The permeability was approximately negatively correlated with volumetric strain. With an increase in gas pressure, the threshold value of the damage factor increases gradually, and the initial damage point of the sample gradually moves backward. At a pressure of 2 MPa, the degree of damage to the sample was relatively large. After failure, the internal cracks in the specimen developed and expanded rapidly, resulting in an upward trend in permeability. At pressures of 2.5 and 3 MPa, although the yield failure generated new cracks, owing to a decrease in cementation strength between particles and particle separation, shear slip blocked some natural leakage channels, resulting in an unclear permeability variation range. In the postpeak stage, the increasing volumetric strain caused the sample to continue to densify, and the permeability of the sample further decreased. When gas pressure was applied, it was equivalent to the axial prestress of the sample. The greater the gas pressure, the smaller the shear stress of the sample when it entered the yield state. After the yield, the sample was continuously subjected to a larger three-way pressure, resulting in a longer plastic-stage duration.

Keywords: true triaxial stress, coal sample, seepage, strength characteristics, failure characteristics, yield condition

Highlights

1. The deformation, seepage, damage, strength, and failure characteristics of coal samples under true triaxial loading–unloading conditions were analyzed using various means.
2. The reason why the permeability of the sample continues to decrease after damage was analyzed.
3. The influence of gas pressure on the yield condition of the sample was analyzed.

Variable annotations

Variate	Annotation	Variate	Annotation
τ_{oct}	Octahedral shear stress (MPa)	E	Elasticity modulus (GPa)
σ_1	The maximum principal stresses (MPa)	v	Poisson's ratio
σ_2	The intermediate principal stresses (MPa)	D	Damage variable
σ_3	The minimum principal stresses (MPa)	Y	The generalized shear strain (10^{-2})
ε	Strain (10^{-2})	$\sigma_{m,2}$	The average effective normal stress
ε_1	Strain value in σ_1 direction corresponding to the peak of τ_{oct} (10^{-2})	σ_c	Uniaxial compressive strength (MPa)
ε_2	Strain value in σ_2 direction corresponding to	c	Cohesion (MPa)

	the peak of τ_{oct} (10^{-2})		
ε_3	Strain value in σ_3 direction corresponding to the peak of τ_{oct} (10^{-2})	φ	Internal friction angle (°)
k	Permeability (m^2)	I_1	The first invariants of deviatoric stress
p, q, θ_σ	The stress states of samples under true triaxial loading–unloading	J_2	The second invariants of deviatoric stress

1. Introduction

In underground engineering, the rock mass is in the stress state of the original rock before excavation. Mining stress is an important force that causes the deformation and failure of rock masses in various underground engineering applications, such as mining and tunnels. As shown in Figure 1, during the tunneling of the working face, the stress environment of the surrounding rock mass changes significantly, which is manifested as the unloading of horizontal stress and the increase in vertical stress. Therefore, it is important to study the failure and deformation characteristics of coal samples caused by true triaxial stress loading and unloading under seepage conditions, which is crucial for roadway support and surrounding-rock control in underground projects, such as coal mines.

Researchers worldwide have extensively studied the mechanical properties of coal and rock under true triaxial stress—for example, the influence of the stress path on rock mechanical properties, influence of true triaxial loading and unloading on coal permeability, and deformation and failure characteristics of rock under the action of loading and unloading stress.

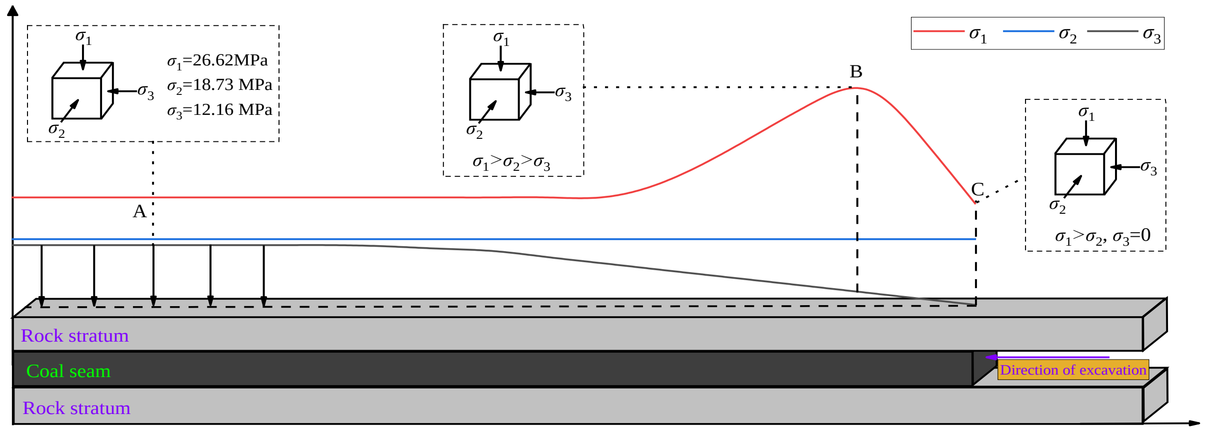

Figure 1. Stress environment of rock mass in front of driving face

Regarding the influence of stress paths on the mechanical properties of rocks, Li et al. (2016) studied shale permeability under anisotropic true triaxial stress. Feng et al. (2020) performed different loading–unloading stress path tests under a true triaxial compression condition and investigated thoroughly the strength, deformation, and failure mechanisms of Jinping marble. Bai et al. (2019) conducted a true triaxial acoustic emission experiment and applied the calculated stress path to a cubic granite sample to simulate rock damage in the roof. Xiao et al. (2020) conducted many complicated unloading tests incorporating a stress unloading path using a true triaxial test system and investigated the effects of prior cyclic loading damage in rocks on subsequent unloading failure characteristics. The deformation, strength, and failure characteristics of soft sandstone and raw coal were investigated by Lu et al. (2020) under two true triaxial loading paths using a self-developed true triaxial test apparatus. Liang et al. (2022) conducted true triaxial conventional loading, true triaxial gradient cyclic loading and unloading, and true triaxial main stress rotation path tests to reveal mechanical behaviors and failure characteristics. Wang et al. (2019) simulated the mechanical behavior of granular materials under a complex stress loading path using a new numerical true triaxial engine and provided the stress–strain responses of a type of typical granular sand under several stress loading paths in meridian and deviatoric stress spaces.

Many studies have been conducted on the effects of true triaxial loading and unloading on rock permeability (Lombosl et al., 2013; Kwasniewski et al., 2013). Alexeev et al. (2004) applied the designed lap true triaxial test device to the prediction of coal and gas outbursts and determined the influence of water content on those outbursts. The true triaxial pressure chamber developed by Haimson et al. (2000) can be used to determine the deformation and strength of rocks under water injection pressure. Nasseri et al. (2014) designed and developed a true triaxial test device for synchronous testing of loading, temperature control, and permeability tests. Yin et al. (2015) conducted stress–strain–seepage coupling and hydraulic fracturing tests of coarse sandstone under the condition of true triaxial stress using a multifunctional true triaxial fluid–solid coupling test system. Experiments were conducted by Liu et al. (2019a, 2019b) on different stratifications based on coal gas permeability, and they determined the mechanisms of stress change that influence fissure evolution in stratified coal under true triaxial conditions. Bedding direction was found to have a significant effect on the seepage characteristics of coal samples. Li et al. (2019) conducted a true triaxial geomechanical model test based on the engineering background of the Xiema Tunnel in Chongqing Province to monitor the displacement, stress, and seepage pressure in different monitoring sections. Duan et al. (2019) performed mechanical and seepage experiments on bedded coal using a multifunctional true triaxial geophysical apparatus. They studied the influence of the anisotropy of the coal structure and stress state on the evolution of permeability. Lin et al. (2021) proposed a numerical method to investigate the effects of pore pressure, triaxial stress, and natural fracture failure on shale rock permeability. The results show that, after most of the natural fractures failed under high stress or high pressure, the shale permeability decreases as the stress increases. Yu et al. (2021) investigated the anisotropic characteristics of the effective stress coefficient of sandstone under different pore pressure conditions. The results showed that an increase in pore pressure could cause sandstone particles that block the seepage channel to migrate and reduce the sensitivity of permeability to principal stress. Richards et al. (2012) conducted field and laboratory mixed soil tests in a new true triaxial test apparatus to assess the factors that influence the initiation of piping in noncohesive and cohesive soils. An increase in the maximum principal stress and seepage angle and a decrease in the void ratio caused an increase in the critical seepage velocity. Wu et al. (2021) studied the influence of the three-dimensional seepage water pressure on the shear and compression deformation of a rock mass. The test results showed that changes in the water pressure could cause obvious shear deformation of the interlayer dislocation zone and tensile deformation. Yu et al. (2022a, 2022b) investigated the influence of induced damage on the effective stress coefficient and permeability of sandstones under true triaxial stress. The effective stress coefficient and permeability are closely related to the damage evolution and fracture propagation.

Finally, in terms of rock deformation and failure, Li et al. (2011) studied the expansion deformation of coal after gas adsorption. This indicates that the higher the proportion of adsorbed gas in coal, the more significant the expansion deformation of coal. The gas pressure was positively correlated with the expansion deformation of coal. Li et al. (2021) revealed the deformation and failure process and evolution law of fractured rock mass and analyzed the semiquantitative indices of fracture development, such as shape, quantity, density, size, distribution range, spatial position, and rock mass movement angle. Jiang et al. (2021) conducted true triaxial compression tests using different σ_3 values. The characteristic stresses and failure modes of the specimens under different σ_3 values were systematically investigated. Feng et al. (2019) conducted a series of true triaxial tests on sandstone and granite samples, and the results indicated that the deformation, failure strength, and failure mode depended significantly on the stress state.

Although extensive research has been conducted on the mechanical properties of rock under true triaxial stress, research on the loading and unloading of coal samples under different paths and seepage conditions remains insufficient. Therefore, using the coal sample as the research object, a multifunctional true triaxial fluid–solid coupling system was used to simulate the stress state at a mining depth of 200 m; then, a loading and unloading test of the coal sample was performed to analyze the mechanical and deformation characteristics of the coal sample under seepage conditions, and the fracture evolution law was obtained by computed tomography (CT) scanning. This study provides a reference for working face excavation and oil exploitation.

2.Materials and Methods

2.1 Sample Preparation

The coal samples used herein were collected from the Jinzhong coal mine in Yibin, Sichuan Province. The selected coal samples were cut and polished to prepare cube specimens with edge lengths of 100 × 100 × 100 mm, and the flatness of the end face was controlled within 0.02 mm. Simultaneously, to avoid the impact of the end friction effect on the test, a mixed loading method (force–displacement loading) was adopted in this experiment to reduce the end friction effect. In addition, a heat-shrinkable pipe was used to isolate the pressure head, pressurized oil, and specimen, reducing the end effect to some extent. Grease was applied to reduce the friction between the heat-shrinkable tube and the specimen. The surface of the specimen was smooth without evident joints and cracks. A perfectly processed coal specimen is shown in Figure 2.

2.2 Testing Device

1) The true triaxial stress loading and unloading test of coal samples under seepage conditions adopted the multifunctional true triaxial fluid–solid coupling experimental system developed by Chongqing University, as shown in Figure 3 (Li, 2016).

The experimental device included a true three-axis pressure chamber, hydraulic oil pressure system, water or gas seepage system, true three-axis frame and disassembly platform guide rail, pressure, displacement, and flow data monitoring system, and acoustic emission signal monitoring system. The pressure control method of the experimental device ensured that the center point of the cubic coal rock remained unchanged during true triaxial loading. Simultaneously, full rigidity and “1 flexible + 2 rigid” loading were selected for pressure loading, and flexible and rigid loading reduced the end effect. For the true triaxial compression range, the maximum confining pressure was 60 MPa, and the maximum load capacities of the three-way head were 6×10^3, 6×10^3, and 4×10^3 kN, respectively. The test system was used for coal and rock mechanics, seepage, and hydraulic fracturing experiments under different true triaxial stress paths. Meanwhile, a linear variable differential transformer (LVDT) high-precision displacement sensor was used to test the sample deformation, and the mass flowmeter monitored the gas flow in the experimental process in real time.

2) The SOMATOM Cope CT scanning system (Shanghai Siemens Medical Instruments Co., Ltd.) was used for CT scanning. The CT scanning system can be used at any time during the experiment to scan the specimen in the loading chamber, and the evolution of the internal structure of the specimen can be observed and imaged in real time.

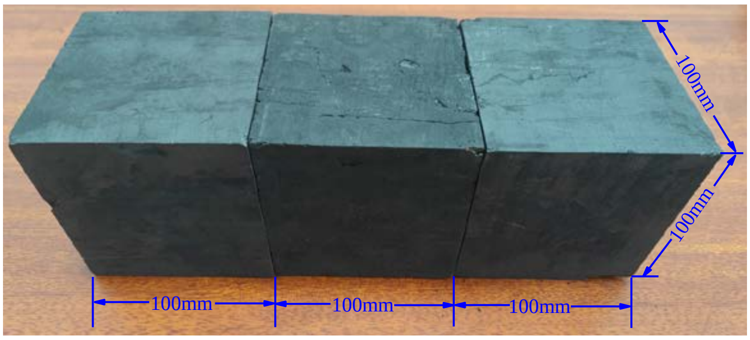

Figure 2. Cubic coal sample

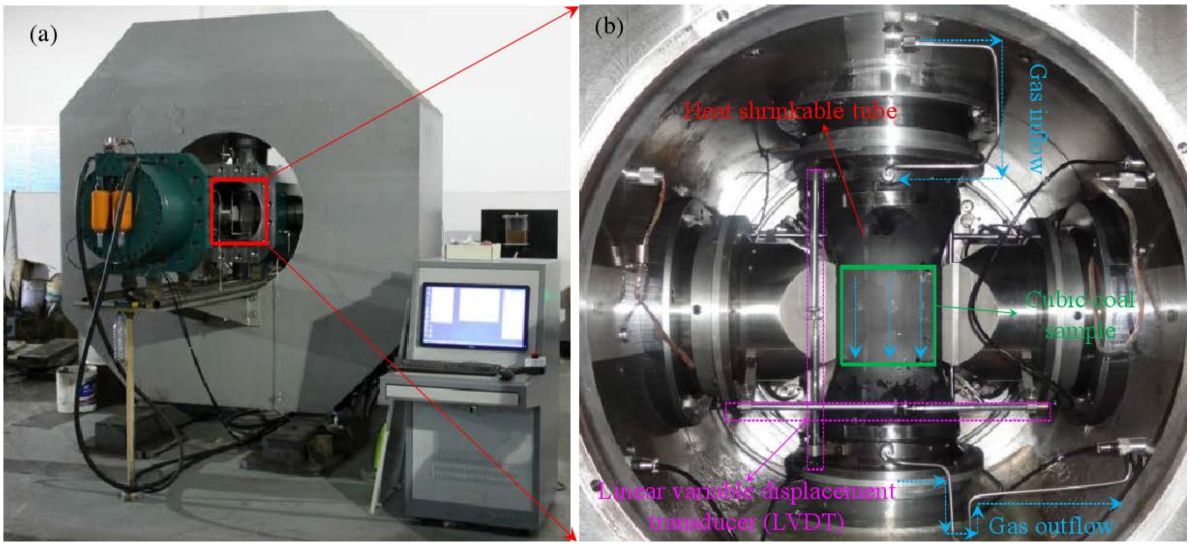

Figure 3. Multifunctional true triaxial fluid-solid coupling experimental system

2.3 Test Method

To study the mechanical properties of coal samples under different seepage conditions more accurately, the initial *in situ* stress states of coal samples obtained according to the field tests were $\sigma_1 = 26.62$, $\sigma_2 = 18.73$, $\sigma_3 = 12.16$ MPa. The sample method is shown in Table 1, and the stress loading path is shown in Figure 4, where σ_t is the principal stress in each direction over time. During the experiment, the seepage direction of the specimens was parallel to the bedding.

In the test, Darcy's law was used to calculate the coal permeability under true triaxial stress loading and unloading conditions, and the formula is

$$k=\frac{2q\mu LP_2}{A(P_1^2-P_2^2)} \tag{1}$$

where k is the permeability (m^2), q is the gas seepage flow under standard conditions (m^3/s), μ is the aerodynamic viscosity (19.9 µPa·s in this study), L is the length of the sample (m), A is the cross-sectional area of the sample (m^2), P_2 is the atmospheric pressure (MPa), and P_1 is the air inlet pressure (MPa).

Table 1: True triaxial loading stress path of coal

Test method	Stress state	Loading paths
Loading steps: 1) Fix the seal oil pressure of 4 MPa (See Figure 11 for the role of oil pressure), load the triaxial principal stress to 7 MPa hydrostatic pressure, and pass in CO_2 gas. (Path 1: 2 MPa; Path 2: 2.5 MPa; Path 3: 3 MPa.) 2) Loading $\sigma_1, \sigma_2, \sigma_3$ at a rate of 2 kN /s to 26.62 MPa, 18.73 MPa, 12.16 MPa. 3) Leave σ_2 unchanged. Unload σ_3 at a rate of 0.03 mm/s. Load σ_1 at a rate of 0.03 mm/s to specimen destruction.	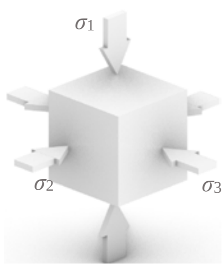	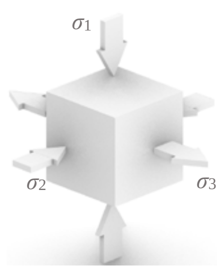

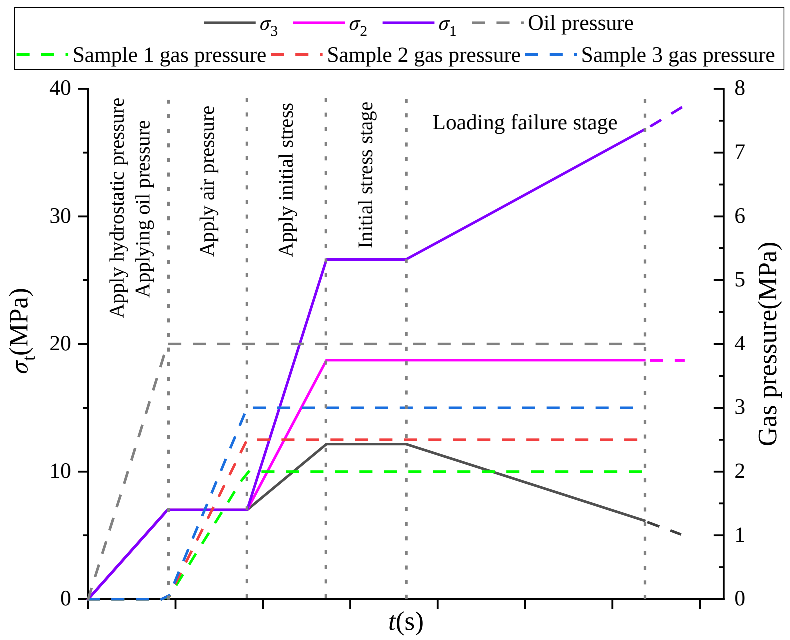

Figure 4. loading path

3. Test Results and Analysis

3.1 Deformation Characteristics

There were certain differences in the stress distribution and deformation inside the surrounding rock of the roadway under different pressure conditions. The deformation characteristics of the coal sample were analyzed, and the corresponding stress–strain and permeability curves are shown in Figure 5.

In Figure 5, τ_{oct} is the octahedral shear stress, i.e., $\frac{1}{3}\sqrt{(\sigma_1-\sigma_3)^2+(\sigma_1-\sigma_2)^2+(\sigma_2-\sigma_3)^2}$, and σ_1, σ_2, and σ_3 are the maximum, intermediate, and minimum principal stresses, respectively. As shown in Figure 5, the deformation in the ε_1 direction is the largest. The mean value of ε_1 at the τ_{oct} peak value is 0.0337, which is 127.3% and 2325% larger than the corresponding mean values of the strain in the ε_3 direction (0.0148) and ε_2 direction (0.00139), respectively. The σ–ε_3 and σ–ε_1 curves are approximately axisymmetric along $\varepsilon = 0$. Compared with the ε_1 and ε_3 directions, the strain in the σ_2 direction is smaller, and its absolute value is less than 5‰. Moreover, during the loading process, the deformation in the σ_2 direction shows a process of compression, expansion, and recompression, resulting in the formation of a σ–ε closed loop. An increase in deformation in the σ_3 direction mainly occurs after the shear stress reaches its peak; then, with continuous loading in the σ_1 direction, the expansion in the σ_3 direction continues to increase. This is because the specimen gradually loses its bearing capacity after failure, and the difference between σ_1 and σ_2 decreases with a decrease in σ_1. However, σ_1 and σ_2 maintain a relatively large difference with σ_3, leading to specimen compression in the σ_1 direction and expansion in the σ_2 and σ_3 directions before failure, and compression in the σ_1 and σ_2 directions and expansion in the σ_3 direction after failure.

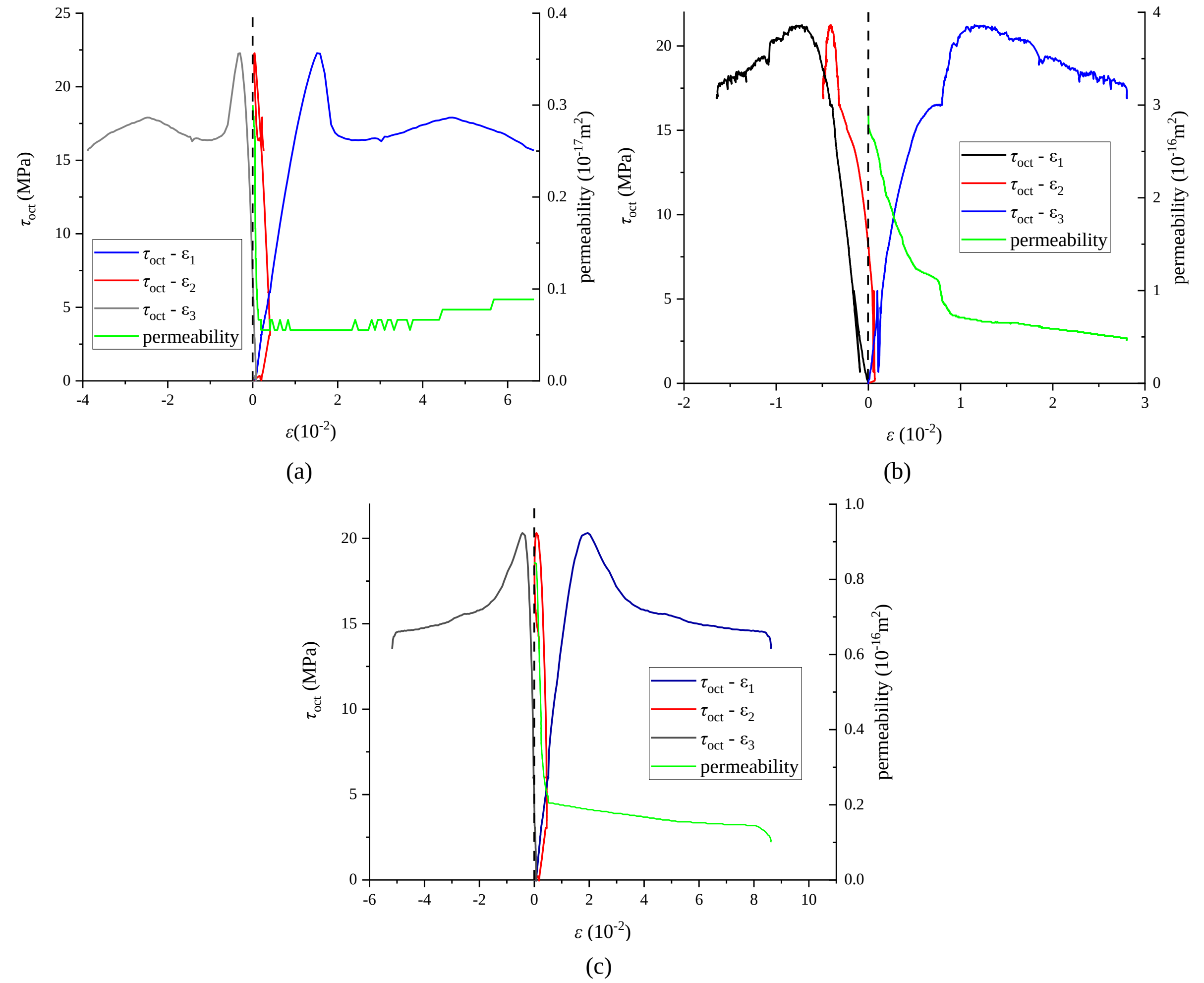

Figure 5. Stress-permeability-strain curve. (a) 2 MPa. (a) 2.5 MPa. (a) 3 MPa

A horizontal comparison for each figure is shown in Figure 5. The trends of the τ_{oct}–ε curves in all directions of the three samples are almost the same, and the τ_{oct}–ε curves show four stages of compaction: linear elasticity, yield, and post-peak. When the pressure is 2 MPa, the peak value of the shear stress is 22.6 MPa, which is 6.6% larger than the peak value of the shear stress (21.2 MPa) at a pressure of 2.5 MPa and 9.2% larger than the peak value of the shear stress (20.7 MPa) at a pressure of 3 MPa, indicating that the strength of the sample is negatively correlated with the gas pressure. This is because the gas pressure affects the effective stress. In the pore space, the effective stress is the difference between the total stress and gas pressure ($\sigma_e = \sigma - p$, where σ_e, σ, and p represent the effective stress, principal stress, and pore pressure, respectively) (Letham et al., 2016). The higher the gas pressure, the lower the effective stress. The decrease in effective stress leads to a decrease in the average normal stress transmitted through the intergranular contact surface in the sample, resulting in a lower shear strength.

3.2 Seepage Characteristic

3.2.1 Analysis of Permeability Variation Characteristics

The permeability parameter characterizes the ability of soil or rock to transmit fluids. Its value is related to porosity, pore geometry, particle size, arrangement direction, and other factors (Ghanbarzadeh, 2016). Analyzing the permeability change rule of each sample in Figure 5 under true triaxial loading and unloading reveals that the permeability change rule of a coal sample under true triaxial loading is different from that under uniaxial loading. Under true triaxial loading and the influence of triaxial pressure and sealing oil pressure, brittle failure of the specimen under uniaxial compression does not occur. After losing the bearing capacity, the coal sample remains in the process of compaction; therefore, the permeability does not increase significantly. To analyze the relationship between permeability and deformation further, the permeability–

shear stress–volumetric strain curve of the sample was drawn (Figure 6). The curve of the sample with a gas pressure of 2.5 MPa is not listed because it is similar to that of the sample with a gas pressure of 3 MPa. Figure 6 shows that, before failure, the permeability of both samples decreases with an increase in deviatoric stress and volumetric strain. However, after failure, the samples with air pressure of 2.5 and 3 MPa have different characteristics from those at 2 MPa; that is, the permeability continues to decrease. In this study, the permeability time curve at 3 MPa (*t*–*x* curve in Figure 6) was taken as an example to analyze the volumetric strain and permeability variation characteristics of the samples at different time periods:

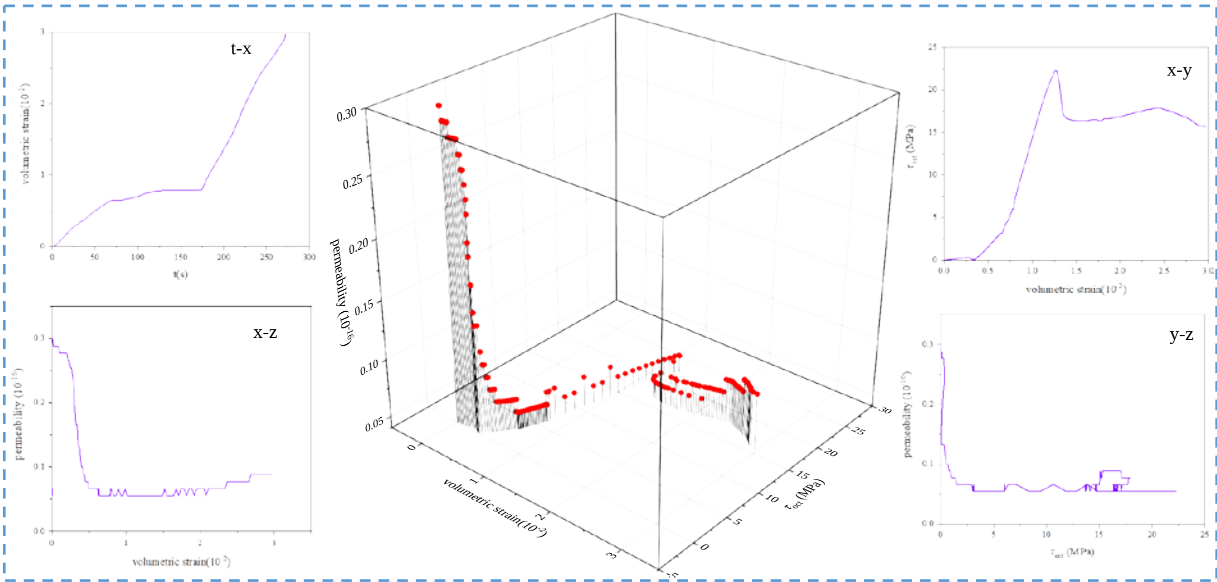

(a)

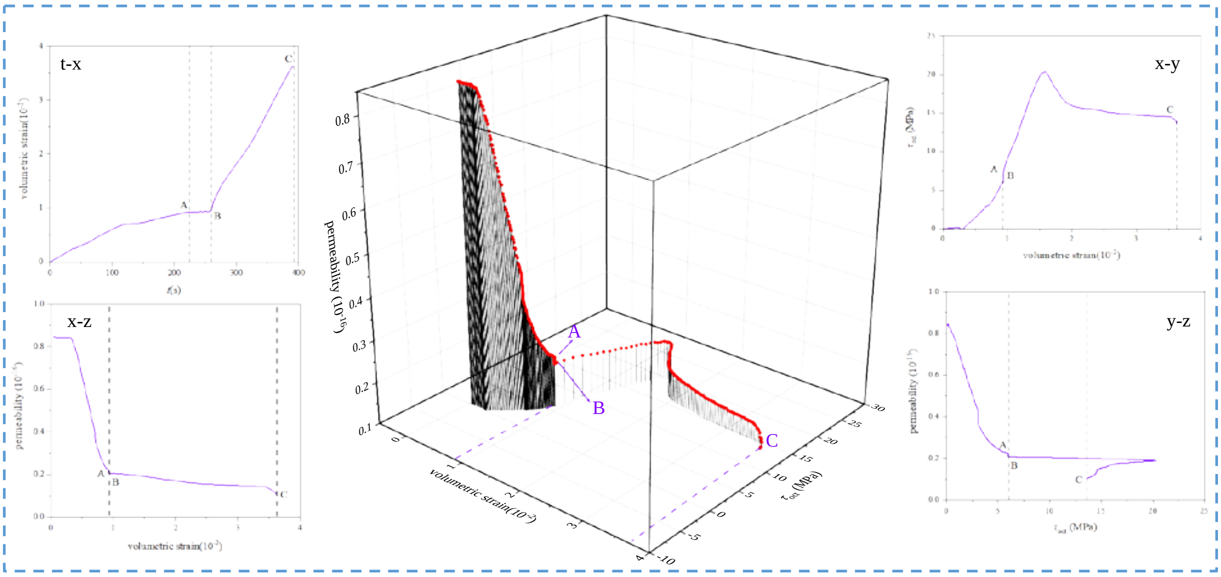

(b)

Figure 6. Permeability - shear stress - volumetric strain - time curve. (a)2 MPa. (b) 3 MPa

1) In the OA segment, i.e., $t \in [0, 225\ \text{s}]$, the volumetric strain of the sample increases gradually with time, but the rate of increase decreases gradually. In particular, when $t \in [200, 225\ \text{s}]$, the curve tends to be flat. At this stage, the permeability of the samples decreases rapidly. An increase in volumetric strain corresponds to a decrease in the sample volume, indicating that the sample is in the compaction stage.

2) In the AB segment, i.e., $t \in [225, 260\ \text{s}]$, the volumetric strain of the sample remains temporarily stable with the extension of time, and this stage corresponds to the elastic stage of the τ_{oct}–ε_V curve. As σ_1 increases, the difference between σ_1 and σ_3 also increases. Under the action of this difference, the sample undergoes elastic deformation, i.e., the maximum principal stress direction compresses, the minimum

principal stress direction expands, and the overall volume of the sample remains basically unchanged. During this phase, the permeability of the samples remains relatively constant.

3) In the BC segment, i.e., $t \in$ [260, 380 s], the shear stress of the sample continues to increase with time. With the continuous increase in shear stress, the sample further compresses in the direction of the maximum principal stress, and the sample breaks when it reaches point C. After point C, the bearing capacity of the sample is lost owing to failure. At this point, the displacement in the direction of the maximum principal stress continues to increase, leading to the rapid collapse of the sample in this direction. Simultaneously, because of an increase in the stress difference, the compression rate of the two directions of the maximum and middle main stresses exceeds the expansion rate of the minimum main stress direction. Therefore, the sample volume shows a trend of continuous decrease, and the permeability of the sample also slowly decreases.

To analyze further the relationship between the sample permeability and volumetric strain, the shear stress and permeability–volumetric-strain curves of the sample are shown in Figure 7, revealing that the permeability of the sample as a whole decreases gradually with an increase in volumetric strain. Taking Figure 7(b) as an example, the permeability–volumetric-strain curve can be divided into two parts by referring to the shear stress–volumetric strain curve.

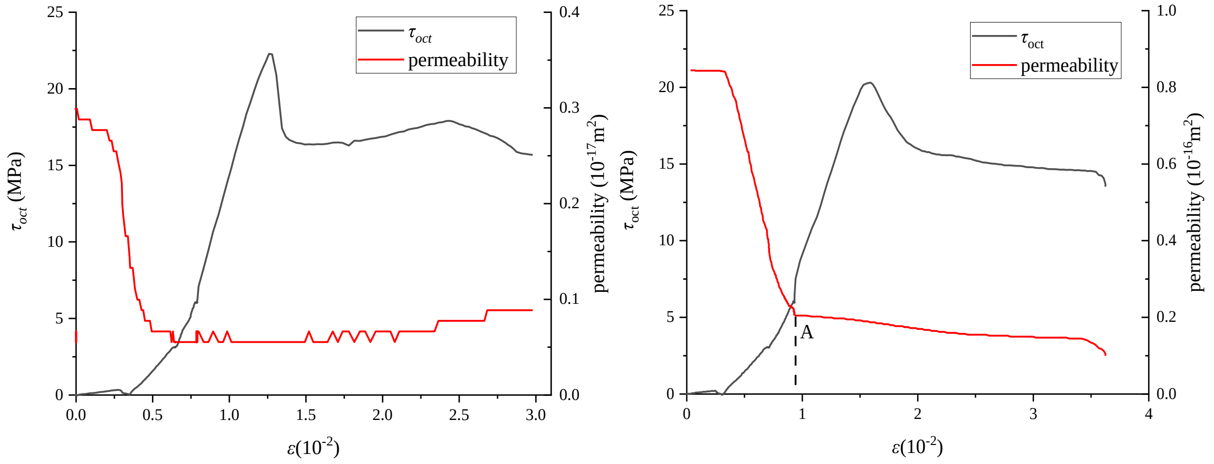

(a) (b)

Figure 7. Shear stress, permeability - volumetric strain curves. (a)2 MPa. (b) 3 MPa

1) Before point A, the permeability decreased rapidly with an increase in the volumetric strain. The shear stress–volumetric strain curve at this stage was mainly in the compaction stage, and the original cracks and pores of the sample were compressed rapidly, resulting in a significant decrease in the permeability of the sample.

2) After point A, the sample begins to be in the elastic stage, the evolution of internal cracks is stable, and the decrease rate of the sample's permeability slows down. When the volumetric strain reached approximately 0.09, the sample cracked; however, because of the slow the unloading direction of the minimum principal stress, the sample was still under a large three-way pressure. As shown in Figure 6, the volume of the sample continued to decrease after failure, resulting in a continuous decrease in the sample’s permeability.

3.2.2 Seepage Model of the Sample Under Different Gas Pressures

Essentially, the change in the stress state is the reason for the change in coal permeability. Therefore, the S–D model considering the coupling effect of stress and seepage can describe the evolution law of coal permeability. The expression for this model has a negative exponential relationship.

$$\frac{k}{k_0} = \mathrm{e}^{-3C_f(\sigma_t-\sigma_0)}, C_f = \frac{1}{K_p} - \frac{1}{K'} \quad (1)$$

where k is the permeability, σ is the effective stress, subscript 0 is the initial state (MPa), C_f is the shear compression coefficient (MPa^{-1}), K_p is the volumetric modulus of the coal crack (MPa), and K is the volumetric modulus of coal (MPa).

Taking the logarithm of both sides of Equation (1) and letting $k_r = \ln(k/k_0)$, Equation (14) can be rewritten as

$$k_r = -3C_f(\sigma_t - \sigma_0). \tag{2}$$

There are many ways to build nonlinear models. The fractional derivative model, which contains the memory effect or historical dependence, has unique advantages. By referring to the fractional modeling idea of non-Darcy seepage (Wang et al., 2017; Zhou et al., 2019; Zhou et al.,2018), a two-parameter fractional permeability model has been established that meets the above conditions (Zhou et al., 2021).

$$k/k_0 = \exp\left\{\xi\left[-\frac{\sigma_t-\sigma_0}{\sigma_L}\right]^{1+\gamma}/\Gamma(2+\gamma)\right\} \tag{3}$$

because

$$\Gamma(x) = \int_0^{+\infty} e^{-t}\, t^{x-1}\, dt = (x-1)\Gamma(x-1) = (x-1)!. \tag{4}$$

Therefore,

$$k/k_0 = \exp\left\{\xi\left[-\frac{\sigma_t-\sigma_0}{\sigma_L}\right]^{1+\gamma}/(1+\gamma)!\right\} \tag{5}$$

For the postfailure stage, $\gamma \neq 0$, there is a difference between the shear stress under true triaxial loading and unloading states and the shear stress under conventional triaxial compression owing to the existence of a constant intermediate principal stress. After substituting the deviational stress under true triaxial conditions, to make it more universal, constants p and q are introduced to represent the offset of Equation (3) in the true triaxial state instead of variable γ; that is,

$$k/k_0 = p + q\cdot\exp\left\{-\frac{\xi\left(\frac{1}{3}\sqrt{(\sigma_1-\sigma_3)^2+(\sigma_1-\sigma_2)^2+(\sigma_2-\sigma_3)^2}\right)}{2}\right\} = p + q\cdot\exp\left\{-\frac{\xi\cdot\sigma}{2}\right\}\ . \tag{6}$$

Equation (6) is used to fit the $k/k_0 - \sigma$ curve, and the result in Figure 8 is obtained.

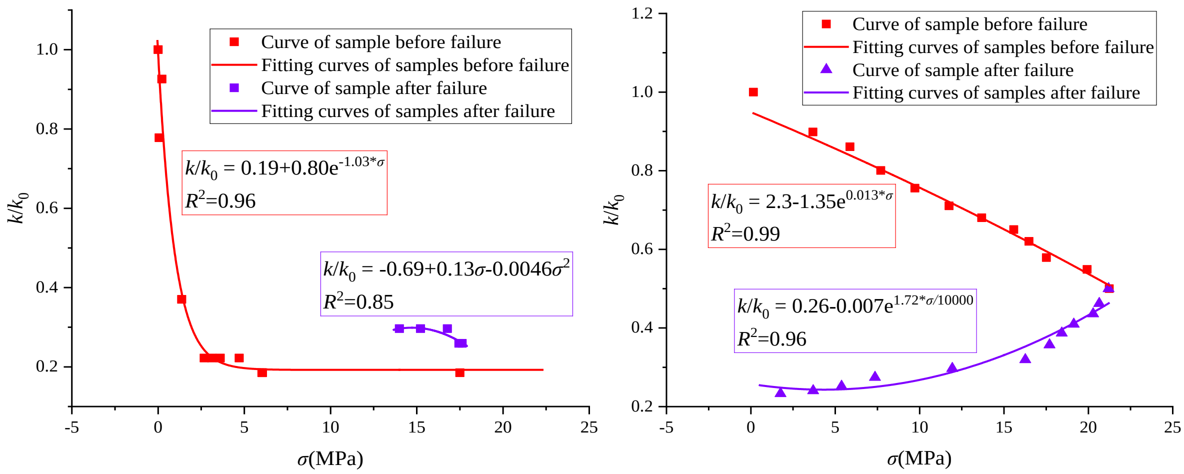

(a) 2 MPa (b) 2.5 MPa

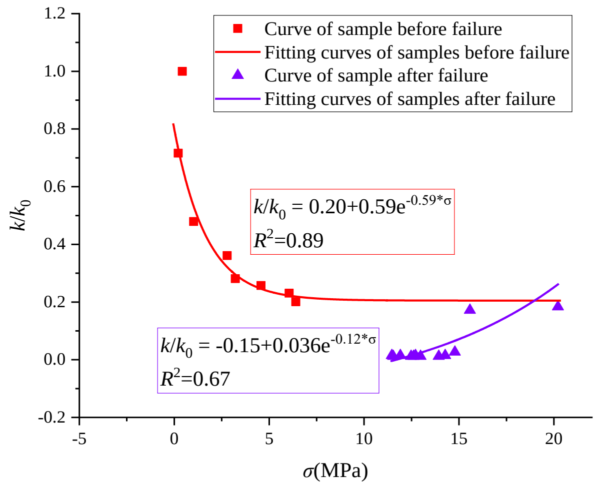

(c) 3 MPa

Figure 8. Permeability model results: (a) 2 MPa, (b) 2.5 MPa, and (c) 3 MPa

Figure 8 shows that the permeability model has a very good fitting effect in the prepeak stage. The determination coefficients R^2 of the three pressure conditions are greater than 0.98. However, the fitting effect of the permeability model is not ideal in the postpeak stage. At 3 MPa, the correlation coefficient of the postpeak fitting curve is only 0.67. At 2 MPa, the exponential function fitting curve does not converge, so polynomial curve fitting is used. This indicates that the established seepage model can adapt well to the nonlinear variation characteristics in the prepeak stage.

3.3 Damage Characteristic

The damage variable represents the degree of deterioration of the sample, which can be intuitively understood as the percentage of the volume of microcracks or voids in the material. In damage mechanics, the damage variable plays the role of "deterioration operator." From a thermodynamic perspective, the damage variable can reflect the irreversible change process of the material structure. Therefore, it is important to calculate the variation rule of the damage variable D of the sample under true triaxial loading and unloading conditions to explore the damage characteristics of the sample.

To obtain the evolution law of damage variables, it is necessary to construct a damage constitutive equation. In continuum damage mechanics, the three-dimensional linear elastic damage constitutive equation can be expressed as (Xie et al., 2004)

$$\varepsilon_{ij} = \frac{1+v}{E}\frac{\gamma_{ij}}{1-D} - \frac{v}{E}\frac{\sigma_{kk}}{1-D}\delta_{ij} \quad (i,j = 1,2,3)\,. \tag{7}$$

According to Equation (7), the damage constitutive equation of rock under a true triaxial loading path can be obtained as

$$\sigma_1 = v\sigma_2 + v\sigma_3 + E(1-D)\varepsilon_1. \tag{8}$$

The expression of the damage variable D is based on the damage evolution equation of concrete material under compression proposed by Mazars (Mazars et al., 1986), which is easy to use and in line with the hypothesis in this study that the peak point is the starting point of damage. Its expression is

$$D = 1 - \frac{1}{exp(mY)}, \tag{9}$$

where m is the experimentally determined material parameter and Y is the generalized shear strain, which is

$$Y = \int \sqrt{\frac{2}{3}de:de}\,;\ de = d\varepsilon - tr(\frac{d\varepsilon}{3})\delta \tag{10}$$

The generalized shear strain expression under true triaxial loading path is

$$Y = \sqrt{\frac{2}{9}[(\varepsilon_1-\varepsilon_2)^2 + (\varepsilon_2-\varepsilon_3)^2 + (\varepsilon_3-\varepsilon_1)^2]}\ . \tag{11}$$

Some researchers have modified the Mazars equation by extending the applicable object to rock, better displaying the brittleness–ductility transformation characteristics of rock from low to high confining pressure and improving the fitting accuracy of the rock damage evolution process after the damage threshold. The modified Mazars damage evolution equation is (Mazars 1986)

$$D = 1 - \frac{1}{\exp(mY) + nY} \ . \tag{12}$$

According to the damage constitutive equation and damage evolution equation, the stress–strain curve obtained from the above loading and unloading seepage experiment was fitted to determine the damage evolution parameters (Table 2). The theoretical damage constitutive and damage evolution curves obtained are shown in Figure 9.

Table 2: Damage evolution parameters

Gas pressure (MPa)	*m*	*n*	*E* (GPa)	*v*
2	1.15	0.8	4.72	0.3
2.5	0.72	0.6	4.60	0.3
3	0.7	0.75	2.97	0.3

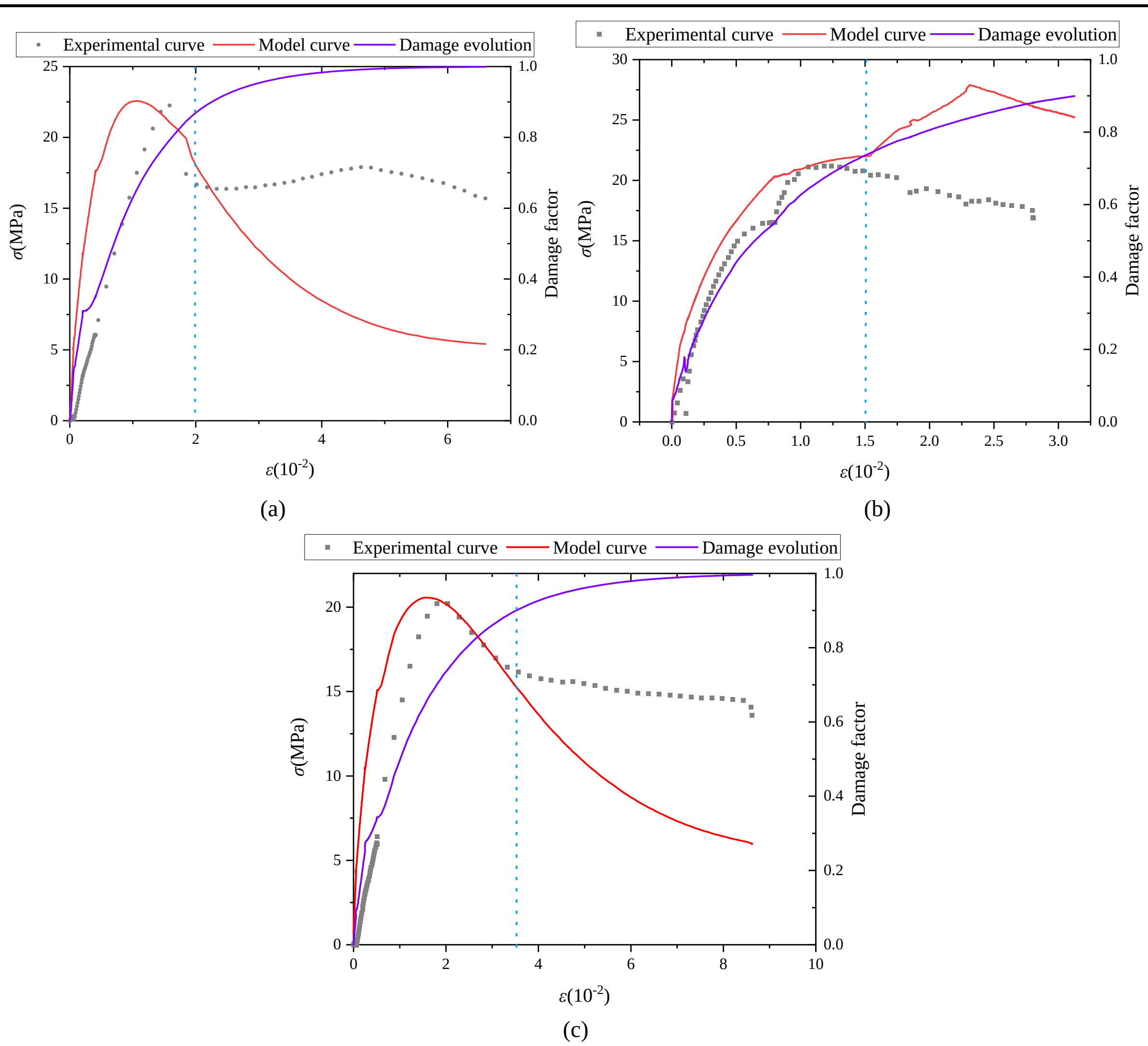

Figure 9. Damage evolution curve: (a) 2 MPa, (b) 2.5 MPa, and (c) 3 MPa

Figure 9 shows that the damage factor of each sample increases slowly in the compaction and elastic stages but increases rapidly when it approaches the yield-to-failure stage. Therefore, the damage of the sample mainly occurs in the yield and failure stages. Comparing Figures 9(a)–(c) shows that, when the gas pressure increases from 2 to 3 MPa, the threshold value of the damage factor of the sample gradually increases. Hence, the initial damage point of the sample gradually moves backward with an increase in gas pressure. The constitutive model agrees well with the test curve before the peak failure.

3.4 Strength Characteristics

At present, the Mohr–Coulomb and Drucker–Prager criteria are generally adopted for rock strength analysis. However, the Mohr–Coulomb criterion does not reflect the influence of the intermediate principal stress on rock strength; therefore, it is not applicable to the description of rock strength under true triaxial stress.

To improve accuracy, the Mogi–Coulomb and Drucker–Prager criteria were used to compare and analyze the strength parameters of rocks under different water pressures in true triaxial tests. The Mogi–Coulomb criterion describes a monotone increasing function relationship between the octahedral shear stress and effective average normal stress.

$$\tau_{oct} = a + b\sigma_{m,2} \tag{13}$$

$$\tau_{oct} = \frac{1}{3}\sqrt{(\sigma_1 - \sigma_3)^2 + (\sigma_1 - \sigma_2)^2 + (\sigma_2 - \sigma_3)^2} \tag{14}$$

$$\sigma_{m,2} = \frac{\sigma_1 + \sigma_3}{2} \tag{15}$$

where τ_{oct} is the octahedral shear stress, $\sigma_{m,2}$ is the average effective normal stress, *a* is the intercept of the fitting line of the Mogi–Coulomb criterion, and *b* is the slope of this line.

The relationship between the Mogi–Coulomb parameters (*a*, *b*) and the parameters of the Mohr–Coulomb criterion is

$$\mathrm{a} = \frac{2\sqrt{2}}{3} c cos\varphi \tag{16}$$

$$\mathrm{b} = \frac{2\sqrt{3}}{3} sin\varphi. \tag{17}$$

The values of τ_{oct} and $\sigma_{m,2}$ for the coal samples are calculated using Equations (14) and (15). The Mogi–Coulomb criterion equation of the coal samples can be obtained using the linear fitting method according to Equation (13).

$$\tau_{oct} = 1.50 + 0.55\sigma_{m,2} \tag{18}$$

The fitting curve is shown in Figure 10(a), and the Mogi–Coulomb criterion a = 1.50, b = 0.55 is substituted into Equations (16) and (17). The Mohr–Coulomb strength parameters of coal can be obtained as c = 1.96 MPa, φ = 35.7°.

The Drucker–Prager criterion is obtained based on the extension of Mohr–Coulomb criterion and Mise criteria in plastic mechanics, and its equation is

$$\sqrt{J_2} = \alpha I_1 + k, \tag{19}$$

where α and *k* are test parameters, I_1 and J_2 are the first and second invariants of stress and deviatoric stress, respectively.

$$I_1 = \sigma_1 + \sigma_2 + \sigma_3 \tag{20}$$

$$J_2 = \frac{1}{6}[(\sigma_1 - \sigma_2)^2 + (\sigma_2 - \sigma_3)^2 + (\sigma_3 - \sigma_1)^2] \tag{21}$$

Considering the plane strain problem, the relationship between the parameters of the Drucker–Prager and Mohr–Coulomb criteria is

$$\alpha = \frac{2tan\varphi}{\sqrt{9 + 12tan^2\varphi}} \tag{22}$$

$$k = \frac{3c}{\sqrt{9 + 12tan^2\varphi}}. \tag{23}$$

The values of I_1 and J_2 for each sample are calculated according to Equations (20) and (21). According to Equation (19), the fitting equation of the Drucker–Prager criterion for the sample can be obtained using the linear fitting method:

$$\sqrt{J_2} = 0.26I_1 + 2.2 \tag{24}$$

The fitting curve is shown in Figure 10(b). From the figure, $\alpha = 0.26$, $k = 2.2$, the Mohr–Coulomb strength parameters $c = 2.46$ MPa, $\varphi = 23.6°$ of the experimental coal can be obtained according to Equations (22) and (23).

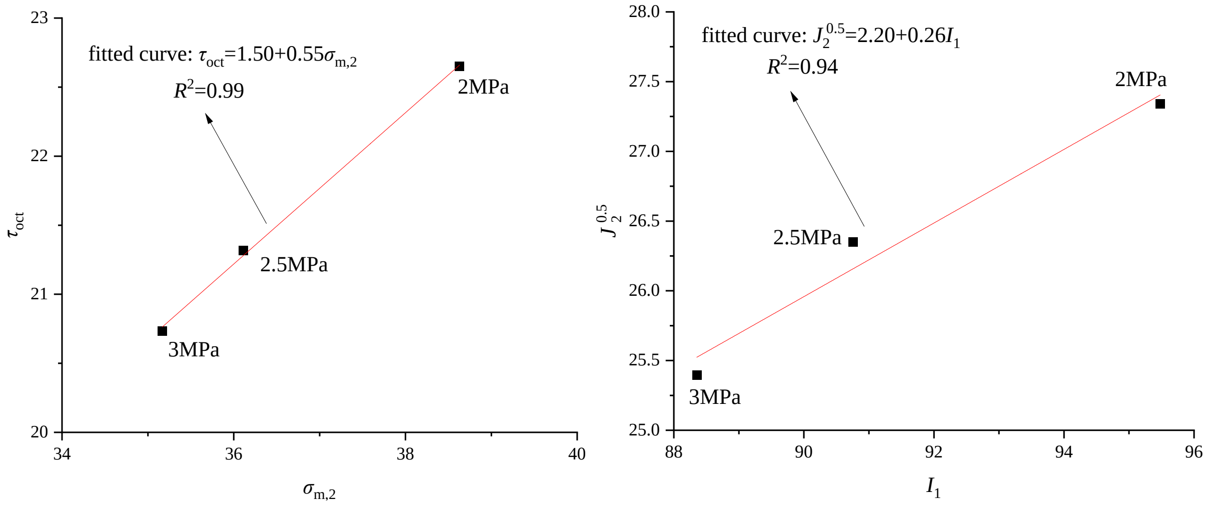

(a) (b)

Figure 10. Mogi-Coulomb and Drucker-Prager guideline fitting curves. (a) Mogi-Coulomb. (b) Drucker-Prager

Figures 10(a) and (b) show that the correlation coefficient R^2 of the fitting curve of the Mogi–Coulomb strength criterion is 0.99 and that of the Drucker–Prager strength criterion is 0.94. Thus, the Mogi–Coulomb strength criterion is more suitable for describing the failure strength characteristics of coal samples under true triaxial seepage. According to the Mohr–Coulomb strength criterion, the mechanical parameters of the samples are $c = 1.96$ MPa, $\varphi = 35.7°$.

3.5 Failure Characteristics

The failure characteristics and fracture evolution law of rocks are important for analyzing the failure mechanism of rocks (Ramsay, 1980) and are crucial for analyzing the variation characteristics of permeability under true triaxial loading (Sprunt, 1979). The sample with seepage failure was scanned by CT, and the scanning files were processed using 3D Slicer software to synthesize the three-dimensional map of the sample and extract the surface and internal slices to conduct an in-depth analysis of its failure characteristics. The results are presented in Table 3, where the z-direction is the direction of the intermediate principal stress, the x-direction is the direction of the minimum principal stress, and the y-direction is the direction of the maximum principal stress. Face y in the x-direction is the section perpendicular to the y-direction obtained from the sample tangential to the x-direction.

According to the longitudinal comparison of each sample in Table 3, the section length along the y-direction is the longest, the section length along the z-direction is in the middle, and the section length along the x-direction is the shortest. The y-direction is the direction of the maximum principal stress, and the length of the section in this direction is smaller than that in the other directions, indicating that the strain in this direction is mainly compressed. The z-direction is the direction of the intermediate principal stress, and the length of the section in this direction is close to that before the test, indicating that the deformation in this direction is relatively small. The x-direction is the direction of the minimum principal stress, and the length of the section in this direction is the largest, indicating that the strain in this direction is mainly expansion. These results are consistent with the above analysis.

Table 3: CT scanning images of coal samples destroyed under seepage condition

Sample	Direction	Face	Depth: 15mm, 40mm, 65mm, 90mm.
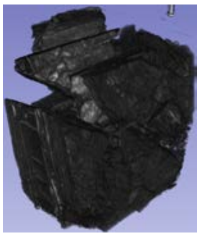 CO_2 2 MPa	x (σ_3)	y	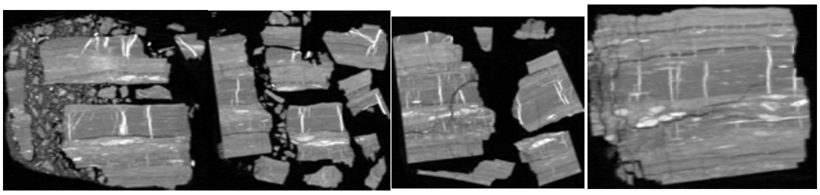
	z (σ_2)	x	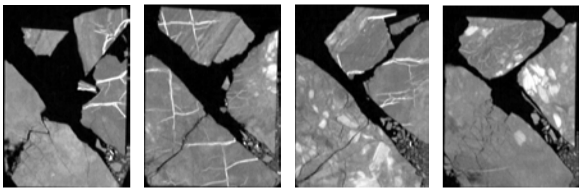
	y (σ_1)	z	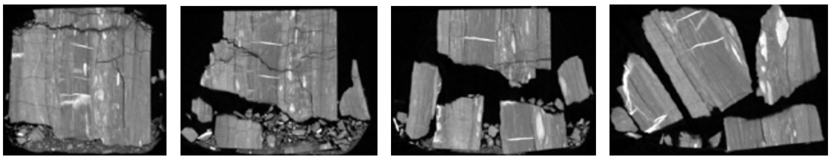
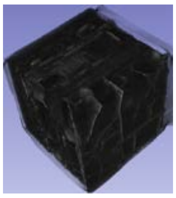 CO_2 2.5 MPa	x (σ_3)	y	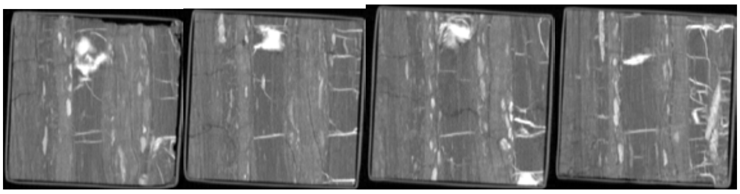
	z (σ_2)	x	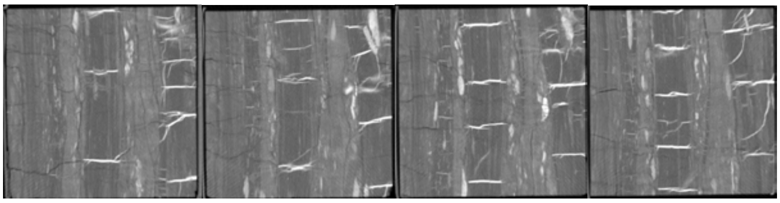
	y (σ_1)	z	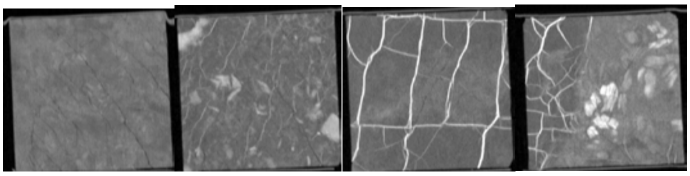
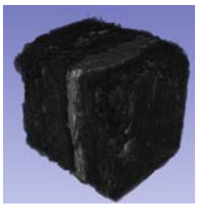 CO_2 3 MPa	x (σ_3)	y	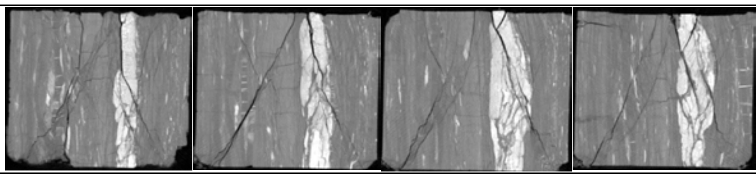
	z (σ_2)	x	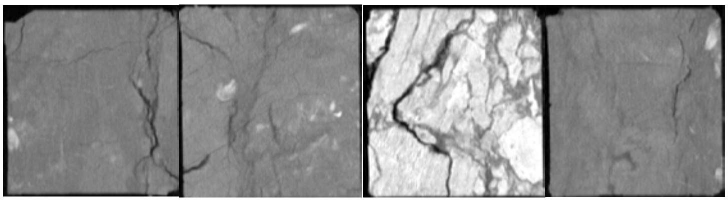
	y (σ_1)	z	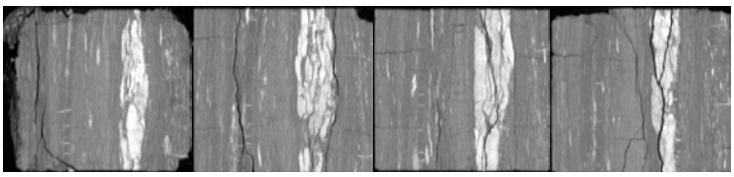

A coal sample is a typical heterogeneous material, and its failure process is the formation, development, convergence, and localized failure process of microcracks. The shape of the fracture section is primarily affected by the physical properties and stress state of the coal itself. When the failure characteristics of the sample were observed at a pressure of 3 MPa, vertical and inclined cracks appeared on the failure plane perpendicular to the σ_1 and σ_2 directions, representing the appearance of tensile and shear cracks. In particular, on the failure plane perpendicular to the σ_1 direction, the fracture density was the largest, and the expansion was more obvious. Most fractures were parallel to σ_2 and pointed in the σ_3 direction. Arc-shaped cracks appeared on the failure surface perpendicular to the σ_2 direction, which oscillated repeatedly with an increase in cutting depth, and a complex shear seam network appeared, corresponding to folded cracks in the σ_1 direction. This was because the stress in the σ_1 direction was the largest. When the specimen was fractured, the cracks first sprouted in the plane perpendicular to the σ_1 direction and then gradually expanded. Because the stress in the σ_3 direction was the smallest, cracks developed and expanded in this direction more easily. Consequently, several cracks pointing in the σ_3 direction appeared in the plane perpendicular to the σ_1 direction.

The failure characteristics of the sample with a pressure of 2.5 MPa are not obvious because the shear stress of the sample decreases sharply after failure and is caused by three-way compaction. By careful observation of the failure surface perpendicular to σ_2, relatively dense inclined cracks can be observed on the positive side. With an increase in the cutting depth, the cracks gradually disappear, indicating that no crack structure formed in this direction. Corresponding vertical cracks also formed on the surface perpendicular to σ_1 and σ_2, indicating that the main body failure mode of the sample was shear failure.

Observing the failure characteristics of the sample at a pressure of 2 MPa revealed that this group of samples is different from the other two groups. Obvious damage occurred during seepage compression, and the fracture of the sample was extended and integrated, especially in the failure surface in the σ_1 and σ_2 directions. On the failure plane perpendicular to the σ_3 direction, an obvious shear failure occurred. With an increase in penetration depth, the failure mode gradually changed from X-type conjugate failure to Y-type shear failure. This phenomenon demonstrated that the true triaxial loading and unloading test under the condition of CO_2 seepage caused shear failure in the coal sample. With a decrease in gas pressure, the effective stress increased gradually, and the shear failure characteristics tended to be more obvious.

4. Discussion

4.1 Analysis of Volumetric Strain and Permeability Evolution Characteristics of the Samples

In typical tests, the volume of coal and rock samples tends to increase after failure, resulting in increased permeability, which is also reflected in this study. As discussed in Section 3.1, when the air pressure was 2 MPa, the permeability of the sample continued to decline before failure but increased significantly after the failure. This is the result of the failure of the sample and the continuous expansion of cracks, which can also be observed from the failure characteristics in Section 3.5.

However, in the experiment, another phenomenon was observed. As reported in Section 3.2, the volume change characteristics of the samples are compression–smooth-transition–recompression. Under gas pressures of 2.5 and 3 MPa, the permeability of the samples did not increase after failure but continued to decrease. From the analysis of the failure characteristics, the failure pattern of the sample at 2.5 and 3 MPa was completely different from that at 2 MPa, and no obvious breakage occurred. A schematic diagram of the anisotropic strain and particle change of the sample at an air pressure of 3 MPa is shown in Figure 11. (Because the deformation of the principal stress direction in the middle is relatively small, the deformation in this direction is not marked on the cube diagram in the figure.) From a macroscopic viewpoint, continuous axial compression causes the specimen to be compressed in the vertical direction, and its compression speed exceeds the expansion speed in the horizontal direction, resulting in a continuous reduction in specimen volume. From a microscopic viewpoint, after the sample loses its bearing capacity, the continuous axial compression accelerates the internal collapse of the sample, reducing the cementation strength between particles in the sample and leading to particle separation and shear slip. As a result, the natural seepage channels, such as the original bedding and cleat, are blocked, further reducing the permeability.

In addition, with the triaxial stress of the sample reaching hydrostatic pressure as the starting point, the change rule of the volumetric strain of the sample at a pressure of 3 MPa was analyzed further. With an increase in the triaxial principal stress, the volumetric strain of the sample first increased and then tended to flatten. After the specimen reached the initial *in situ* stress condition, the deformation of the specimen in the σ_2 and σ_3 directions continued to increase owing to the continuous compression in the σ_1 direction, and the volumetric strain of the specimen also increased rapidly. However, unlike the stress–strain curve, the deformation–time curve of the specimen did not show an obvious turning point owing to the fracture of the specimen. This indicates that, although the bearing stress of the specimen decreased with a continuous increase in displacement after failure, the overall deformation of the specimen continued, and the volume strain kept increasing. Volume compression confirmed the dislocation and closure of cracks. In this experiment, the seepage direction was parallel to the bedding; therefore, the specimen failure led to an increase in the curvature of the seepage channel, while the three-way compression limited the expansion of new cracks. This also led to a downward trend in penetration. The test results and analysis indicate that the permeability of the sample did not necessarily increase with the fracture of the sample. For coal or soft rock under three-way compression, permeability can continue to decrease after failure.

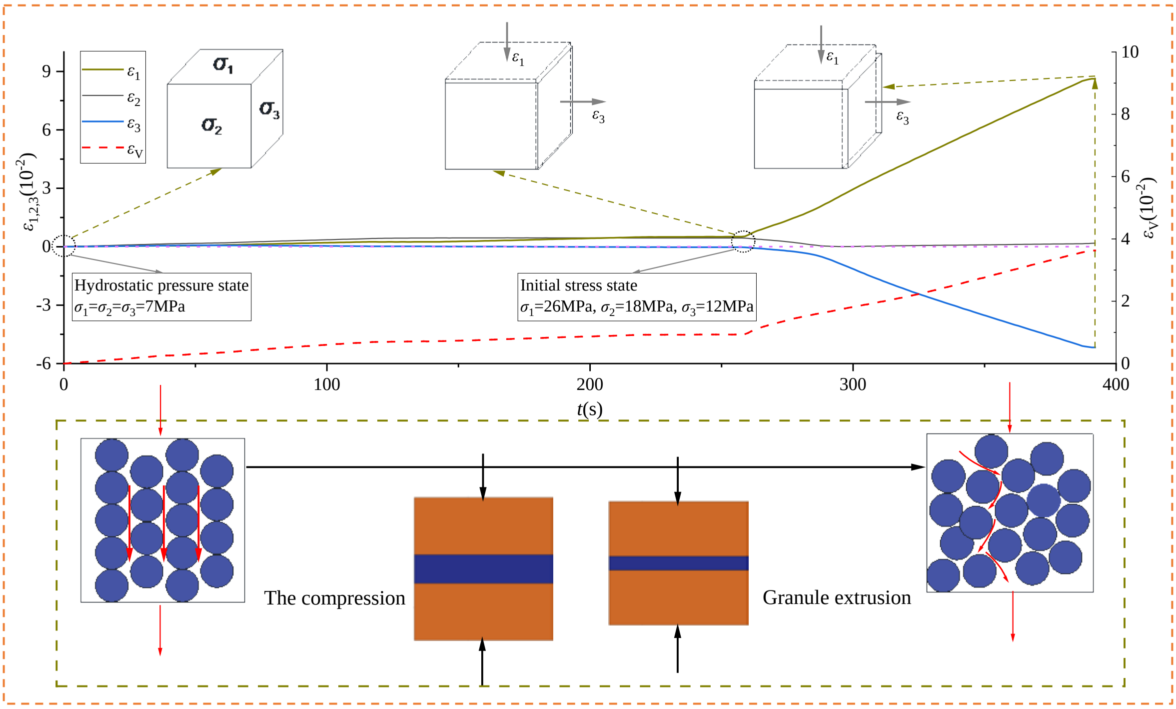

Figure 11. Mechanism of volumetric strain variation under true triaxial compression

4.2 Analysis of Yield Conditions Under Different Gas Pressures

The yield condition is the boundary point between the elastic and plastic states, i.e., the limit of the elastic state. The coal sample had low strength and obvious plasticity, and most of the coal samples had active development of natural joints and strong anisotropy. The uniaxial compression curve showed a significant prepeak jitter and difference, and an elastic or plastic stage was not obvious from the uniaxial compression stress–strain curve alone. It was also difficult to distinguish obvious yield conditions. In Section 3.3, the damage characteristics of the samples were analyzed under true triaxial loading from the perspective of strain. Therefore, based on the results in Sections 3.3 and 3.4, no attempt was made to explore the variation characteristics of the yield conditions of samples under different gas pressures from the perspective of stress by applying the three-dimensional energy yield conditions of geotechnical materials.

Zheng et al. (2020) proposed a three-dimensional energy yield condition based on the traditional three-dimensional molar stress circle:

$$psin\varphi + \frac{q}{3}\left(\sqrt{3}cos\theta_\sigma - sin\theta_\sigma sin\varphi\right) = c \cdot cos\varphi \tag{25}$$

In Equation (25), p, q, θ_σ represent the stress states of the coal samples under true triaxial loading and unloading:

$$\begin{cases} p = \dfrac{\sigma_1 + \sigma_2 + \sigma_3}{3} \\ q = \dfrac{\sqrt{(\sigma_1 - \sigma_2)^2 + (\sigma_1 - \sigma_3)^2 + (\sigma_2 - \sigma_3)^2}}{\sqrt{2}} \\ \theta_\sigma = \arctan\left[\dfrac{2\sigma_2 - \sigma_1 - \sigma_3}{\sqrt{3}(\sigma_1 - \sigma_3)}\right] \end{cases}$$

The function $y = f(p, q, \theta_\sigma)$ is constructed to discuss the stress state of the sample when it reaches yield, namely,

$$y = f(p, q, \theta_\sigma) = psin\varphi + \frac{q}{3}\left(\sqrt{3}cos\theta_\sigma - sin\theta_\sigma sin\varphi\right). \tag{26}$$

Then, it is clear when the sample yields

$$y|_{Yield} = f(p, q, \theta_\sigma)|_{Yield} = c \cdot cos\varphi = 1.59 \tag{27}$$

According to Equation (26), y values of the sample under various stress conditions with time changes were calculated, and a three-dimensional diagram of the yield conditions was constructed (Figure 12). Because the four-dimensional space cannot be expressed, Figure 12 shows a three-dimensional image $\{y, p, q\}$ and the relationship between y and p, q. In the figure, the blue area represents plane $y = 1.59$. When the $y = f(p, q, \theta_\sigma)$ curve passes through this plane from top to bottom, it indicates that the sample is entering the yield stage.

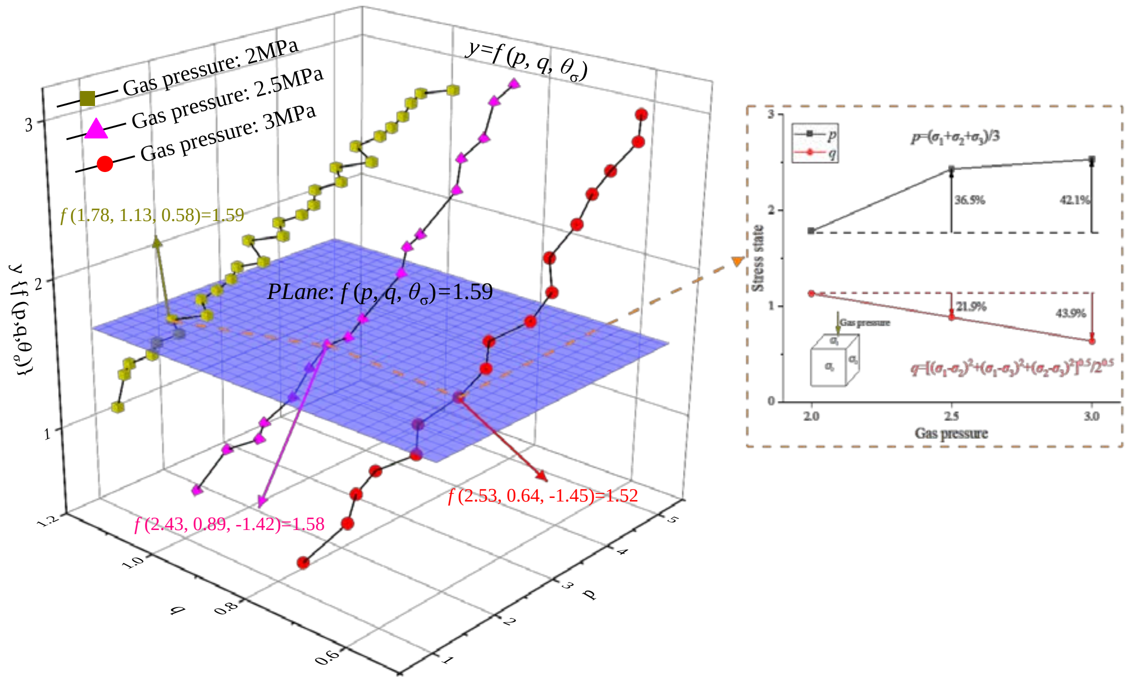

Figure 12. Yield conditions of samples under different air pressures

Figure 12 shows that gas pressure has a great influence on the sample. Abscissa p in Figure 12 is a function of the sum of three principal stresses, and the ordinate q has a linear relationship with the octahedral shear stress τ_{oct}. With an increase in gas pressure, p increases first and then flattens, while q decreases almost linearly. Therefore, the higher the gas pressure, the smaller the shear stress when the sample enters the yield state. However, there is no obvious linear relationship between the sum of the three principal stresses and the gas pressure. This is because the strength of the coal sample is low, and the axial gas pressure has a significant impact on the mechanical properties of coal before the application of triaxial principal stress. If the gas pressure is regarded as the prestress imposed on the axial direction of the coal sample, the higher the gas pressure before loading, the greater the prestress of the sample, and the more easily the sample enters the yield stage after loading. After yielding, the sample is subjected to a large three-way pressure owing to continuous oil pressure and principal stress, resulting in a long plastic stage until the final failure.

4.3 Numerical Simulation Verification

In Section 3.5, the failure characteristics of the sample under different pressure seeps were analyzed. Although the sample was removed in time after the test and a CT scan was performed, oil immersion or block shedding inevitably occurred during the process of loading, unloading, and transferring. To explore the failure mechanism of the samples under seepage conditions further, 3DEC software was used to simulate coal samples under true triaxial loading and unloading.

The model was divided into seven parts: the coal samples and six indenters. The indenter is composed of a cuboid and a trapezoidal body. The dimensions of the cuboid are approximately 100 × 100 × 40 mm. The height of the trapezoidal body part is 10 mm, and the size of the contact surface with the sample is 90 × 90 mm. The indenter is linear elastic constitutive and isotropic by default, and sliding and tensile damage cannot occur. The size of the coal sample is 100 × 100 × 100 mm, which is consistent with the sample size in the laboratory test. This is set as the Mohr–Coulomb constitutive model. According to the calculation results of the Mogi–Coulomb strength criterion in Section 3.2 and the data in Table 2, the strength parameters formulated are listed in Table 4.

3DEC software was used to simulate the force, deformation, and failure characteristics of the coal body, and the model was established (Figure 13), where block 1 is the sample, blocks 2 and 3 are indenters in the direction of minimum principal stress, blocks 4 and 5 are indenters in the direction of intermediate principal stress, and blocks 6 and 7 are indenters in the direction of the maximum principal stress.

Table 4: Mechanical parameters of coal seam roof and floor

Group	Gas pressure/MPa	c/MPa	$\varphi/^\circ$	E/GPa	Tensile Strength/MPa
1	2	1.96	35.7	2.97	0.95
2	2.5	1.96	35.7	4.60	0.95
3	3	1.96	35.7	4.72	0.95

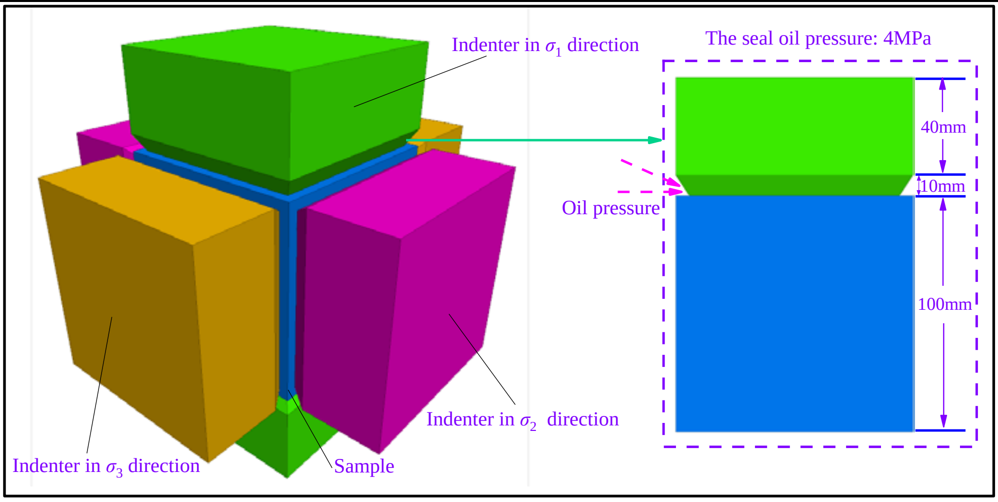

Figure 13. 3DEC model

A cylinder with a bottom diameter of 10 mm and height of 100 mm was drawn at the surface center of the coal sample perpendicular to the direction of the maximum principal stress. CO_2 pressures of 2, 2.5, and 3 MPa were applied to the upper surface of the cylinder. The boundary conditions of the model are as follows: the fixed left, down, and front indenters are zero in each direction to constrain the model; the tangential speed of the right, back, and upper indenters are fixed as 0 to prevent the displacement of the head outside the normal direction when adding and unloading and then produce shear stress on the sample surface, such as τ_{xz} and τ_{yz}; and the gap between the indenter and the sample is sealed with an oil pressure of 4 MPa. To simplify the calculation process, the initial stress is applied after the gas pressure is applied:

insitu stress <*sxx*, *syy*, *szz*, *sxy*, *sxz*, *syz*> = <-12.16e6, -26.62e6, -18.73e6, 0, 0, 0>

Because the force of the block under the action of the testing machine is not completely uniform, a stress gradient from the center of the block to each surface is added (in the model, the center of the sample is the origin).

$$\begin{cases} \text{xgrad} < sxxx, syyx, szzx, sxyx, sxzx, syzx > = < 5, 5, 5, 0, 0, 0 > \\ \text{ygrad} < sxxy, syyy, szzy, sxyy, sxzy, syzy > = < 5, 5, 5, 0, 0, 0 > \\ \text{zgrad} < sxxz, syyz, szzz, sxyz, sxzz, syzz > = < 5, 5, 5, 0, 0, 0 > \end{cases}$$

The stress distribution applied to the coal body is expressed in Equation (27), where σ_{xx}^0 is the stress at the origin of the coordinates.

$$\begin{cases} \sigma_{xx} = \sigma_{xx}^0 + (sxxx) * x + (sxxy) * y + (sxxz) * z \\ \sigma_{yy} = \sigma_{yy}^0 + (syyx) * x + (syyy) * y + (syyz) * z \\ \sigma_{zz} = \sigma_{zz}^0 + (szzx) * x + (szzy) * y + (szzz) * z \end{cases} \quad (27)$$

After the initial stress was applied, loading and unloading tests of the sample were performed using the Fish language. First, the normal velocity is released in the σ_2-direction, and then the σ_2-direction stress remains unchanged (i.e., the displacement boundary is changed to the stress boundary). Then, the σ_1-direction is loaded at a speed of −0.03 mm/s; simultaneously, the σ_3-direction is unloaded at a speed of 0.003 mm/s (the default compression value is negative). Before the calculation started, five measuring points were arranged on each positive surface of the sample, and 15 measuring points were used to monitor the normal stress and normal displacement of each surface. The distribution of the measurement points is shown in Figure 14.

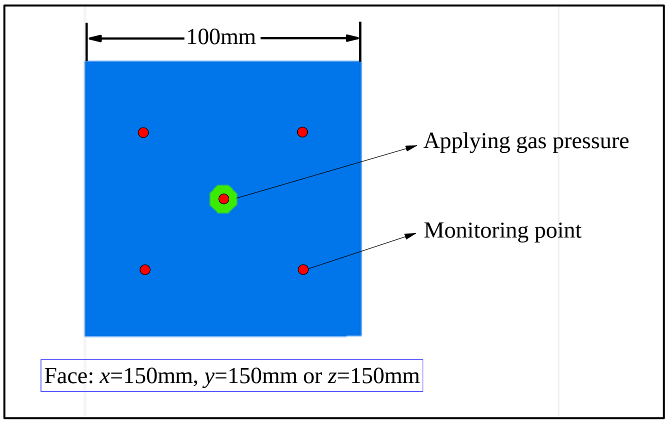

Figure 14. Arrangement of Monitoring points

The normal stress and normal displacement of each surface were extracted, and the curve shown in Figure 15 was drawn. The values of the stress and strain are the average values of the five measuring points on the same surface. Because the applied initial stress σ^T=(26.62MPa, 18.73 MPa, 12.16 MPa)^T, according to the shear stress calculation formula $\sigma=\sqrt{(\sigma_1-\sigma_3)^2+(\sigma_1-\sigma_2)^2+(\sigma_2-\sigma_3)^2/3}$, the shear stress starting point of the numerical simulation curve is σ = 5.91 MPa.

Figure 15 reveals that the trend of the stress–strain curve of the numerical simulation is similar to the model curve in Section 3.3, and both are close to the indoor test curve before the peak. However, because the starting point of the former shear stress is not at the zero point, there is a certain deviation in the initial stage. The curve after the peak is quite different from the test curve, which shows a sharp decrease in the residual strength after the peak because the intermediate principal stress cannot be maintained stably during the numerical simulation calculation. As shown in Figure 15, the jitter of the intermediate principal stress in the numerical simulation is more obvious than that in the laboratory test, particularly after the peak value, showing a significant downward trend. This may be related to the failure of the specimen to lose its bearing capacity. The unloading of the minimum principal stress and drop in the intermediate principal stress caused the true triaxial test to change rapidly to the uniaxial loading mode after the peak value of the specimen. A decrease in the confining pressure level leads to an increase in the brittleness of the specimen and a decrease in the postpeak residual strength.

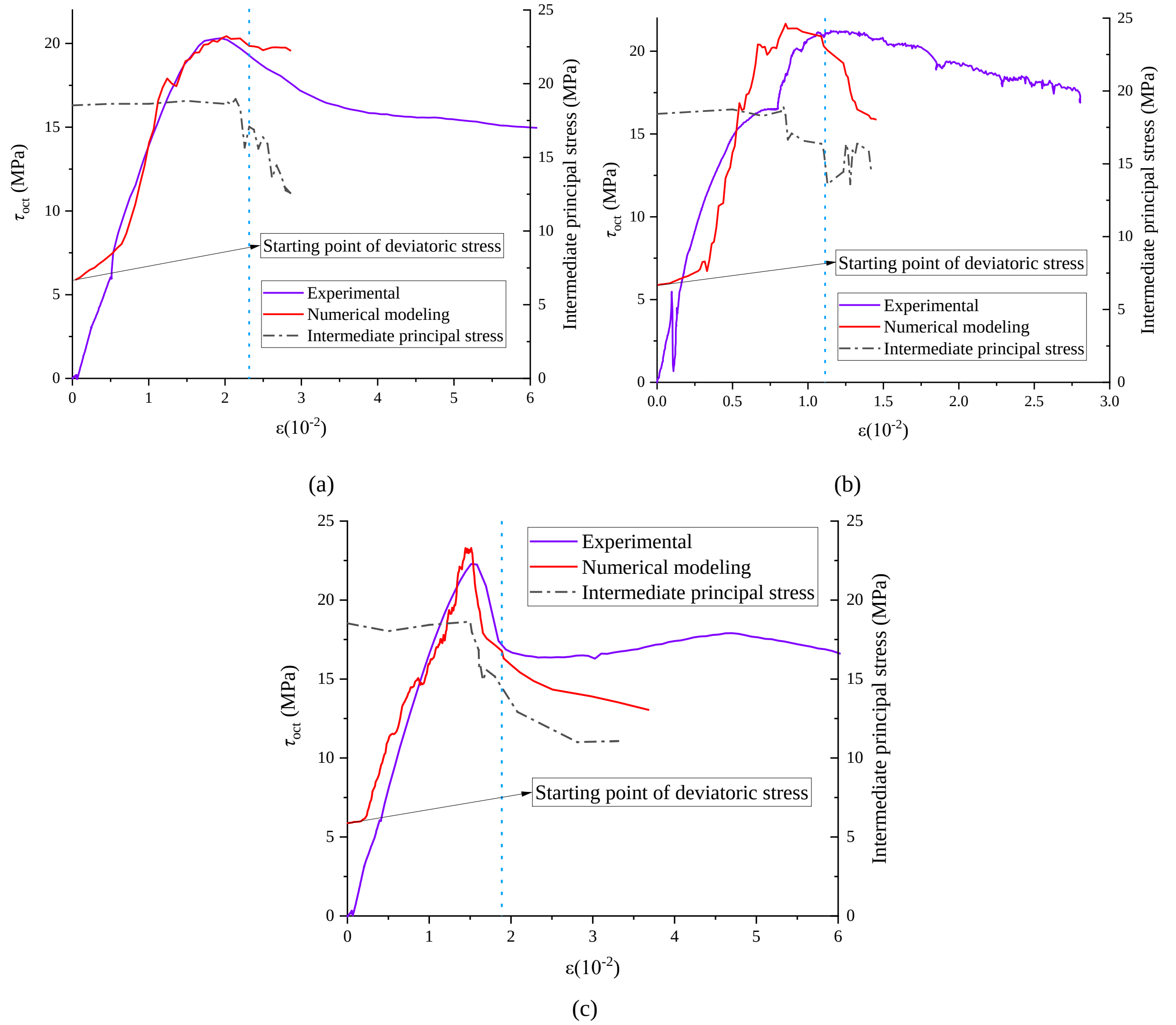

Figure 15. Comparison between numerical simulation and laboratory test results. (a)2 MPa. (b) 2.5 MPa. (c)3 MPa

After the test, positive displacement was applied to each indenter to detach it from the sample, and each indenter was hidden simultaneously. The failure characteristics of the sample are shown in Figure 16.

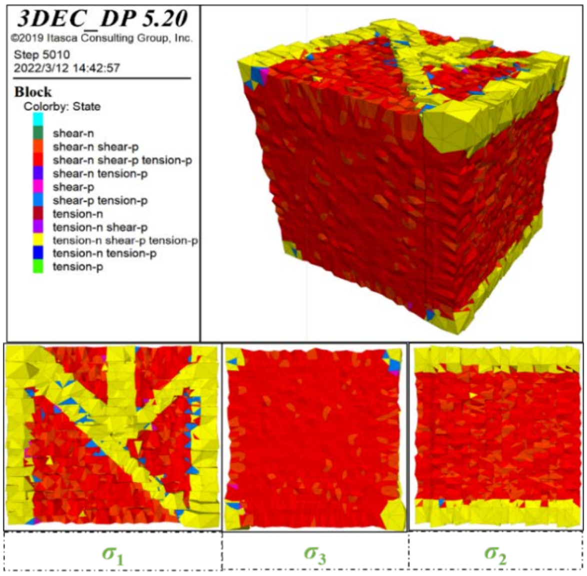

(a)

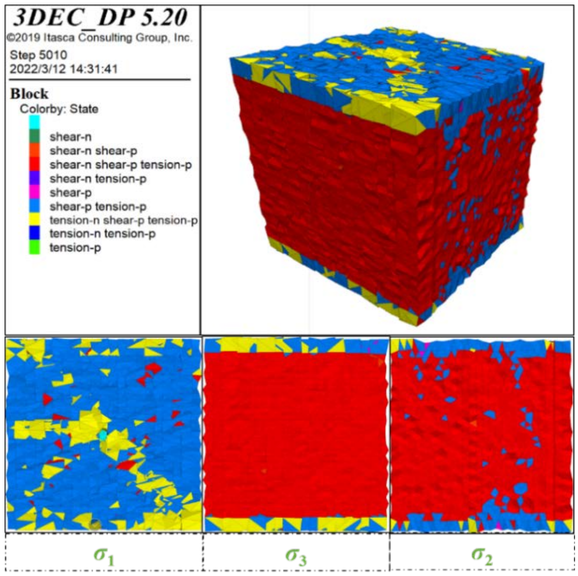

(b)

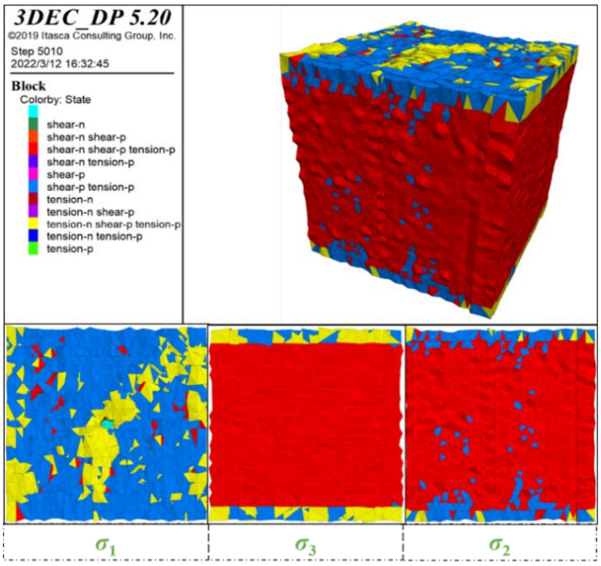

(c)

Figure 16. calculation results of 3DEC. (a)2 MPa. (b) 2.5 MPa. (c)3 MPa

As shown in Figure 16, the failure characteristics of the sample with a gas pressure of 2 MPa are clearly different from those of the other two. On the surface perpendicular to the maximum principal stress, there are obvious diagonal cracks, and the damaged part has obvious protrusions. Therefore, the sample has been damaged, and the cracks expand and penetrate, which is similar to the failure mode of the sample under the laboratory test described in Section 3.4. The sample with a 3-MPa gas pressure has an obvious inclined crack from the upper right corner to the lower left corner of the failure surface perpendicular to the maximum principal stress. There is also sporadic damage on the line between the upper left and the lower right corners, representing the emergence of the prototype of conjugate X-type failure. On the plane perpendicular to the minimum principal stress, many sporadic shear failures tend to run through the plane. The tensile failure is concentrated in two sections on the plane perpendicular to the intermediate principal stress. The failure characteristics of the sample at 2.5 MPa are similar to those at 3 MPa. In addition to an obvious inclined crack on the failure surface perpendicular to the maximum principal stress, there is a tensile failure protruding to the left midpoint, resulting in a Y-shaped failure.

In Section 3.5, the fracture characteristics of the samples after failure are analyzed, but only for the samples after failure. One of the advantages of numerical simulation is that the variation in cracks in the samples during true triaxial loading and unloading can be observed continuously. Taking the sample with a gas pressure of 2 MPa as an example, corresponding to its shear stress–axial strain curve, state pictures of the surface at typical moments or with typical characteristics were captured (Figure 17). The figure can be used to analyze the damage evolution law of the sample with the extension of time (i.e., the prolongation of the calculation step) and further elaborate the damage characteristics of the sample under true triaxial loading and unloading conditions.

As shown in Figure 17, in the direction of the maximum principal stress, an inverted y-shaped fracture zone vaguely appeared at the 1500 steps of the sample. With the continuous loading of maximum principal stress, the fracture characteristics of the sample became more obvious. At 2100 steps, the yellow y-shaped tensile failure band appeared. With an increase in loading steps, the failure band became more concentrated and gradually covered the pores. At 3200 steps, the stress–strain curve entered the postpeak stage, and, with a decrease in the load capacity of the sample, the cracks in this direction further expanded and gradually increased. In the direction of the intermediate and minimum principal stresses, a relatively dense shear fracture network appeared on the surface of the sample and then became full shear failure. With the extension of time, tensile failure began to appear at both ends and corners of the sample surface and gradually intensified after sample fracture. The above results show that, under true triaxial loading and unloading conditions, the failure mode of the sample is mainly shear failure, accompanied by a partially transfixed tensile failure zone.

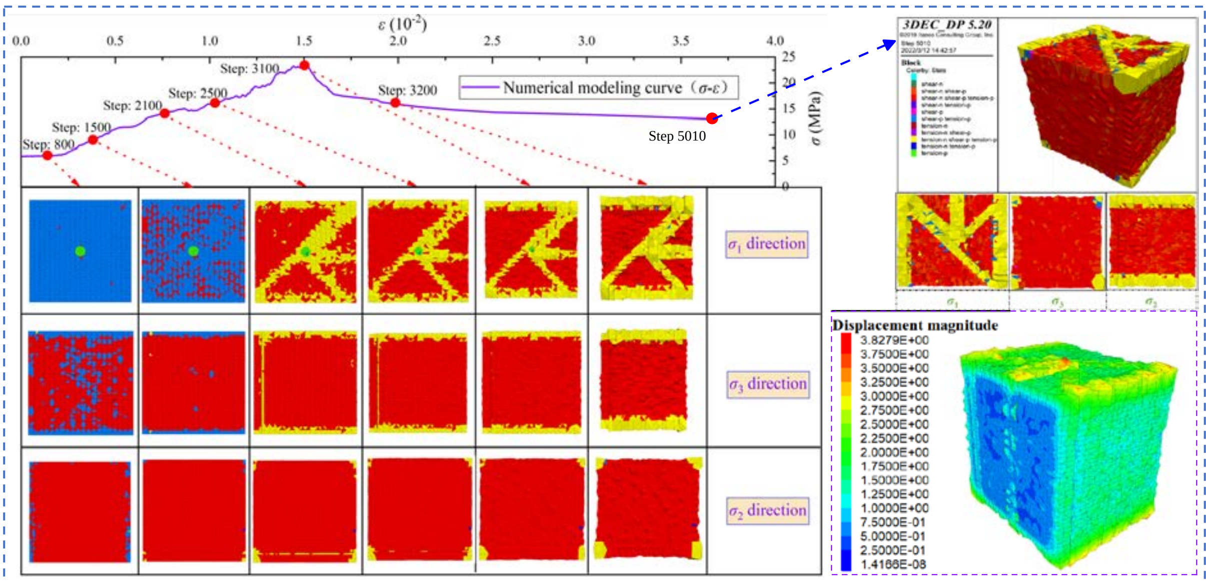

Figure 17. Damage evolution characteristics of samples

In laboratory tests, the volume of the specimen changes with the change in stress, but the indenter does not expand with it. This end face effect not only restricts the deformation of the two ends of the specimen, but also leads to uneven normal stress loading on each surface of the specimen because the edge expansion part is separated from the indenter. In the stress unloading stage, the indenter, which is deep inside the sample, can easily cause secondary damage to the sample when it is raised, resulting in a change in the failure mode of the edge part of the sample. Therefore, the necessary numerical simulation can make conclusions more scientific in laboratory experiments.

5. Conclusion

The deformation, seepage, damage, strength, and failure characteristics of coal samples under true triaxial loading–unloading were analyzed. Based on this, the variation mechanism of the permeability and yield conditions under different gas pressures was investigated. The conclusions are as follows:

1) The volumetric strain over time shows a process of compaction, flattening, and recompaction. The permeability is approximately negatively correlated with the volumetric strain. The increase in gas pressure reduces the effective stress, leading to a decrease in shear strength.

2) Compared with the Drucker–Prager strength criterion, the Mogi–Coulomb strength criterion is more suitable for describing the failure strength characteristics of coal samples under true triaxial seepage. According to the Mohr–Coulomb strength criterion, the mechanical parameters of the samples are c = 1.96 MPa, φ = 35.7°.

3) With an increase in gas pressure, the threshold value of the damage factor increases gradually, and the initial damage point of the sample gradually moves backward. The constitutive model agrees well with the test curve before the peak failure.

4) At a pressure of 2 MPa, the degree of damage to the sample was relatively large. After failure, the internal cracks in the specimen developed and expanded rapidly, resulting in an upward trend in permeability. At pressures of 2.5 and 3 MPa, although the yield failure generated new cracks, owing to a decrease in cementation strength between particles and particle separation, shear slip blocked some natural leakage channels, resulting in an unclear permeability variation range. In the postpeak stage, the increasing volumetric strain caused the sample to continue to densify, and the permeability of the sample further decreased.

5) When gas pressure was applied, it was equivalent to the axial prestress of the sample. The greater the gas pressure, the smaller the shear stress of the sample when it entered the yield state. After the yield, the sample was continuously subjected to a larger three-way pressure, resulting in a longer plastic stage.

6. Statements

6.1 Funding

Supported by Scientific Research Foundation of State Key Lab of Coal Mine Disaster Dynamics and Control. (Project Approval Number: 2011DA105287-zd201804)

6.2 Competing Interests

The authors have no relevant financial or non-financial interests to disclose.

6.3 Author Contributions

Zhang Dongming supervised the research and proposed the research direction. Wang Chongyang was responsible for report analysis and paper writing. Yu Beichen and Li Shujian helped in writing the paper.

6.4 Data Availability

The datasets generated during and analyzed during the current study are available from the corresponding author on reasonable request.

Reference

Alexeev A., Revva V., Alyshev N., (2004). True triaxial loading apparatus and its application to coal outburst predication. *International Journal of Coal Geology*, 58(4): 245–250. https://doi.org/10.1016/j.coal.2003.09.007.

Bai Q., Tibbo M., Nasseri M., Young R., (2019). True triaxial experimental investigation of rock response around the mine-by tunnel under an in situ 3D stress path. *Rock Mechanics and Rock Engineering.* 52(10), 3971-3986. https://doi.org/10.1007/s00603-019-01824-6.

Duan M., Jiang C., Gan Q., Zhao H., Yang Y., Li Z. (2019). Study on permeability anisotropy of bedded coal under true triaxial stress and its application. *Transport In Porous Media.* 131(3), 1007-1035. https://doi.org/10.1007/s11242-019-01375-y.

Feng X., Kong R., Zhang X., Yang C.,(2019). Experimental Study of Failure Differences in Hard Rock Under True Triaxial Compression. *Rock Mechanics and Rock Engineering*. 52(7), 2109-2122. https://doi.org/

10.1007/s00603-018-1700-1.

Feng X., Xu H., Yang C., Zhang X., Gao Y., (2020). Influence of loading and unloading stress paths on the deformation and failure features of Jinping marble under true triaxial compression. *Rock Mechanics and Rock Engineering.* 53(7), 3287-3301. https://doi.org/10.1007/s00603-020-02104-4.

Frash L., Gutierrez M., Hampton J., (2014). True-triaxial apparatus for simulation of hydraulically fractured multi-borehole hot dry rock reservoirs, *International Journal of Rock Mechanics and Mining Sciences*, 70: 496- 506. https://doi.org/10.1016/j.ijrmms.2014.05.017.

Ghanbarzadeh S., Hesse M., Prodanovic M., Gardner J., (2016). Deformation-assisted fluid percolation in rock salt. *Science*. 350(6264), 1069-1072. https://doi. org/10.1126/science.aac8747.

Haimson B., Chang C., (2000). A new true triaxial cell for testing mechanical properties of rock, and its use to determine rock strength and deformability of Westerly granite. *International Journal of Rock Mechanics and Mining Sciences*. 37(1)：285–296. https://doi.org/10.1016/S1365-1609(99)00106-9.

Jiang J., Feng X., Yang C., Su G., (2021). Failure characteristics of surrounding rocks along the radial direction of underground excavations: An experimental study. *Engineering Geology.* 281. https://doi. org/10.1016/j.enggeo.2020.105984.

Kwasniewski M., Li X., Takahashi M., (2013). True triaxial testing of rocks. *London：Taylor and Francis*, 35-49. https://doi.org/10.1201/b12705.

Letham E., Bustin R., (2016). The impact of gas slippage on permeability effective stress laws: implications for predicting permeability of fine-grained lithologies. *International Journal of Coal Geology.* 167: 93-102. https://doi.org/10.1016/j.coal.2016.09.015.

Li M., Yin G., Xu J., Cao J., Song Z., (2016). Permeability evolution of shale under anisotropic true triaxial stress conditions, *International Journal of Coal Geology*, 165: 142-148. https://doi.org/10.1016/j.coal. 2016.08.017.

Li M., Yin G., Xu J., Li W., Song Z., Jiang C., (2016). A Novel True Triaxial Apparatus to Study the Geomechanical and Fluid Flow Aspects of Energy Exploitations in Geological Formations. *Rock Mechanics and Rock Engineering.* 49(12):4647–4659. https://doi.org/10.1007/s00603-016-1060-7.

Li S., Gao C., Zhou Z., Li L., Wang M., Yuan Y., Wang J., (2019). Analysis on the Precursor Information of Water Inrush in Karst Tunnels: A True Triaxial Model Test Study. *Rock Mechanics and Rock Engineering.* 52(2), 373-384. https://doi.org/10.1007/s00603-018-1582-2.

Li X., Li Q., Hu Y., Teng L., Yang S., (2021). Evolution Characteristics of Mining Fissures in Overlying Strata of Stope after Converting from Open-Pit to Underground. *Arabian Journal of Geosciences*. 14(24): 1-18. https://doi.org/10.1007/s12517-021-08978-0.

Li X., Nie B., He X., Zhang X., Yang T., (2011). Influence of gas adsorption on coal body. *Journal of China coal society*, 36(12):2035-2038. https://doi.org/10.13225/j.cnki.jccs.2011.12.016. (In Chinese)

Liang Y., Ran Q., Zou Q., Zhang B., Hong Y., (2022). Experimental Study of Mechanical Behaviors and Failure Characteristics of Coal Under True Triaxial Cyclic Loading and Unloading and Stress Rotation. *Natural Resources Research*. 31(2), 971-991. https://doi.org/10.1007/s11053-022-10022-1.

Lin R., Ren L., Zhao J., Tan X., Rasouli V., Wang X., Wu J., Song Y., Shen C., (2021). Stress and pressure dependent permeability of shale rock: Discrete element method (DEM) simulation on digital core. *Journal of Petroleum Science and Engineering*. 208. https://doi.org/10.1016/j.petrol. 2021.109797.

Liu J., Gao J., Zhang X., Jia G., Wang D., (2019a). Experimental Study of the Seepage Characteristics of Loaded Coal Under True Triaxial Conditions. *Rock Mechanics and Rock Engineering.*52(8), 2815-2833. https://doi.org/10.1007/s00603-018-1720-x.

Liu Y., Yin G., Li M., Zhang., D., Deng B., Liu C., Lu J., (2019b). Anisotropic Mechanical Properties and the Permeability Evolution of Cubic Coal Under True Triaxial Stress Paths. *Rock Mechanics and Rock Engineering.*52(8), 2505-2521. https://doi.org/10.1007/s00603-019-01748-1.

Lombosl L., Roberts D., King M., (2013). Design and development of integrated true triaxial testing system. *London: Taylor and Francis*, 2013: 35-49.

Lu J., Yin G., Zhang D., Gao H., Li C., Li M., (2020). True triaxial strength and failure characteristics of cubic coal and sandstone under different loading paths. *International Journal of Rock Mechanics and Mining Sciences.* 135. https://doi.org/10.1016/j.ijrmms.2020.104439.

Mazars J. (1986). A description of microscale and macroscale damage of concrete structures. *Engineering Fracture Mechanics*, 25(5): 729-737. https://doi.org/10.1016/0013-7944(86)90036-6.

Nasseri M., Goodfellow S., Lombos L., Young R., (2014). 3-D transport and acoustic properties of Fontainebleau sandstone during true-triaxial deformation experiments. *International Journal of Rock Mechanics and Mining Sciences*, 70, 605-606. https://doi.org/10.1016/j.ijrmms.2014.02.014.

Ramsay J., (1980). Crack-seal mechanism of rock deformation. *Nature*. 284(5752), 135-139. https://doi.org/135-139.10.1038/284135a0.

Richards K., Reddy K. (2012). Experimental investigation of initiation of backward erosion piping in soils. *Geotechnique*. 62(10), 933-942. https://doi.org/10.1680/geot.11.P.058.

Sprunt E., Nur. (1979). Microcracking and healing in granites - new evidence from cathodoluminescence. *Science*. 205(4405), 495-497. https://doi. org/10.1126/science.205.4405. 4950.

Wang R, Zhou H., Zhong J., (2017). The study on non-Darcy seepage equation of low velocity flow. *Scientia Sinica- Physica Mechanica and Astronomica*, 47(6): 80-86. https://doi.org/10.1360/SSPMA2016-00366.

Xie H., Chen Z., (2004). Rock Mechanics. *Beijing: Science Press*, 211-216. (In Chinese)

Xiao F., Jiang D., Wu F., Zou Q., Chen J., Chen B., Sun Z., (2020). Effects of prior cyclic loading damage on failure characteristics of sandstone under true-triaxial unloading conditions. *International Journal of Rock Mechanics and Mining Sciences.* 132. https://doi.org/10.1016/j. ijrmms.2020.104379.

Wang X., Zhang Z., Li J. (2019). Triaxial behavior of granular material under complex loading path by a new numerical true triaxial engine. *Advanced Powder Technology. 30(4).,700-706.* https://doi.org/10.1016/j.apt.2018.12.020.

Wu A., Fan L., Fu X., Zhang Y., Zhong Z., Yu M., (2021). Design and application of hydro-mechanical coupling test system for simulating rock masses in high dam reservoir operations. *International Journal of Rock Mechanics and Mining Sciences.* 140. https://doi.org/10.1016/j. ijrmms.2021.104638.

Yin G., Li M., Xu J., Wang W., Li W., Li X., Song Z., Deng B., (2015). A new multi-functional true triaxial fluid-solid coupling experiment system and its application, *Chinese Journal of Rock Mechanics and Engineering*, 34(12): 2436-2445. https://doi.org/10.13722/j.cnki.jrme.2015.0050. (In Chinese)

Yu B., Liu C., Zhang D., Zhao H., Li M., Liu Y., Yu G., Li H., (2021). Experimental study on the anisotropy of the effective stress coefficient of sandstone under true triaxial stress. *Journal of Natural Gas Science and Engineering*. 84. https://doi.org/10.1016/j.jngse.2020.103651.

Yu B., Zhang D., Li S., Xu B., Liu C., Liu Y., (2022b). Biot's Coefficient and Permeability Evolution of Damaged Anisotropic Coal Subjected to True Triaxial Stress. *Rock Mechanics and Rock Engineering*. https://doi.org/10.1007/s00603-022-03085-2.

Yu B., Zhang D., Xiao W., (2022a). Experimental study on the effective stress law and permeability of damaged sandstone under true triaxial stress. *International Journal of Rock Mechanics and Mining Sciences.* 157. https://doi.org/10.1016/j.ijrmms.2022.105169.

Zheng Y., Kong L., A B., (2020) Strength Theory and Numerical Limit Analysis, *Science Press*, 3:49-50. ISBN: 978-7-03-064464-0. (In Chinese)

Zhou H., Yang S., (2018). Fractional derivative approach to non-Darcian flow in porous media. *Journal of Hydrology*, 566(9): 910-918. https://doi.org/10.1016/j.jhydrol.2018.09.039.

Zhou H., Yang S., Zhang S., (2019). Modeling non-Darcian flow and solute transport in porous media with the Caputo-Fabrizio derivative. *Applied Mathematical Modelling*, 68(4): 603-615. https://doi.org/10.

1016/j.apm.2018.09.042.
Zhou H., Zhao J., Su T., Zhang L., Zhong J., Liu Z., (2021). Characterization of gas flow in backfill mining-induced coal seam using a fractional derivative-based permeability model. *International Journal of Rock Mechanics and Mining Sciences*, 138,104571. https://doi.org/10.1016/j.ijrmms.2020.104571.